EUROGRAPHICS 2026
A. Bönsch and N. Umetani
(Guest Editors)

COMPUTER GRAPHICS *forum*
*Volume 45 (2026), Number 2*
*STAR – State of The Art Report*

# Magnetic Modeling and Simulation for Computer Graphics

Xingyu Ni[†1], Yuechen Zhu[2], Ruicheng Wang[3], and Bin Wang[4]

[1]Inria Saclay, France [2]University of Oxford, UK [3]Georgia Institute of Technology, USA [4]Independent Researcher, China

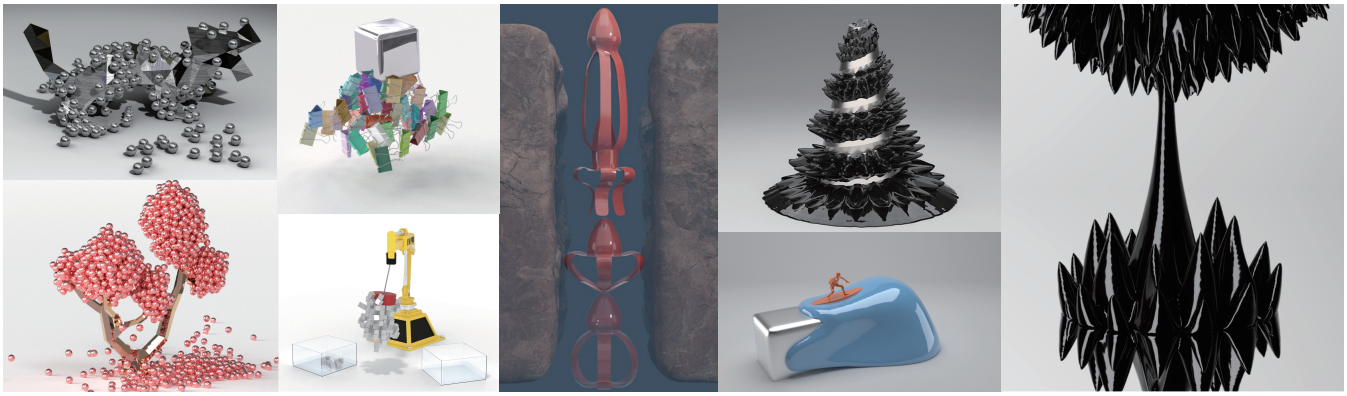

**Figure 1:** *Existing methods can model and simulate various magnetic phenomena for computer graphics applications. The images illustrate, from left to right and top to bottom, magnetically-induced interactions among rigid bodies [TGPS08; KH22; KH20; WFJB24], simulation and control of hard-magnetic thin shells [CNZ*22], and the field-driven behaviors of ferrofluids and magneto-viscoelastic materials [HHM19; SNZ*21; NWWC24].*

**Abstract**

*Physics-based modeling and simulation have long been central to computer graphics, enabling the creation of realistic and expressive digital worlds. While extensive progress has been made in simulating physical phenomena of various materials, magnetic interactions, characterized by their long-range, nonlinear, and material-dependent nature, have only recently attracted sustained attention. Emerging research has explored magnetic effects across rigid bodies, deformable solids, ferrofluids, and magneto-viscoelastic materials, leading to a diverse set of models and solvers. However, these efforts have often evolved in isolation, leaving the broader landscape fragmented. This survey provides the first consolidated perspective on magnetic modeling and simulation for computer graphics. We begin by revisiting the fundamentals of magnetostatics and magneto-mechanical coupling, summarizing the governing equations that underlie existing methods. Building on this foundation, we review numerical algorithms in two complementary aspects: those addressing magnetic fields and magnetization, and those focused on force computation and integration with simulation frameworks. By clarifying common principles and comparing methodological choices, we discuss the successes and challenges of existing literature and outline promising directions for advancing the modeling and simulation of magnetic phenomena.*

**CCS Concepts**

• ***Computing methodologies*** → ***Physical simulation;*** • ***Applied computing*** → *Physics;*

## 1. Introduction

Physics-based modeling and simulation have long been a central topic in computer graphics (CG), enabling the creation of visually compelling and physically plausible animations. Pioneering work such as Terzopoulos et al. [TPBF87] on deformable models, Stam [Sta99] on stable fluid simulations, and Müller et al. [MCG03] on smoothed particle hydrodynamics (SPH) established the foundation for incorporating physics-based methods into graphics applications. These techniques have since been extended to cover a

† Corresponding author

broad spectrum of phenomena, including cloth dynamics [BW98; BFA02], fracture [TF88; PKA*05], granular flows [FSJ01; ZB05], and multiphysics coupling [FAMO99; SSC*13], significantly enriching the realism and versatility of digital worlds. Within this landscape, magnetism represents a relatively new but increasingly active research direction. Unlike classical forces such as contact force, elastic force, or uniform gravity, magnetic interactions are inherently long-ranged, nonlinear, and material-dependent, posing both unique opportunities and computational challenges for the graphics community. Recent years have witnessed a growing body of research dedicated to magnetic modeling and simulation, aiming to expand the repertoire of physics-based animation and to capture visually distinctive effects involving various magnetic materials.

Early efforts in this area include the rigid-body simulations of Thomaszewski et al. [TGPS08], which discretized objects into magnetic dipoles under linear magnetization, but neglected induced fields. Building on this, Kim et al. progressively introduced nonlinear magnetization grounded in micromagnetics [KPH18], reformulated magnetic forces as surface interactions [KH20], and developed differentiable magnetization dynamics to enhance stability and efficiency [KH22]. Chen et al. [CNZ*22] further extended the scope by simulating and controlling hard-magnetic thin shells, coupling magnetic potential energy with St. Venant–Kirchhoff elasticity, and employing a fully implicit Newton solver with adjoint-based differentiation. More recently, Westhofen et al. [WFJB24] coupled magnetic energies with incremental potential contact (IPC) [LFS*20], achieving a strongly coupled simulation of magnetic rigid bodies.

Beyond solid materials, Ishikawa et al. [IYI*13] pioneered procedural magnetic fluid animation based on a SPH analysis. Inspired by this early effort, Huang et al. [HHM19; SHM23] developed a physically grounded SPH framework for ferrofluid simulations, which assumed linear volumetric magnetization and employed volumetric magnetic force models. In parallel, Ni et al. [NZWC20] proposed a unified framework capable of handling rigid bodies, soft bodies, and ferrofluids, using level sets to track material surfaces and modeling magnetic forces as surface interactions. To further improve efficiency, Huang and Michels [HM20] adopted a surface-only liquid solver [DHB*16] combined with boundary element methods (BEM) for magnetic field computation, while Ni et al. [NWWC24] introduced a hybrid approach that couples high-fidelity grid-based fluid solvers with a lightweight boundary-based magnetostatic solver. In addition to typical fluids, Sun et al. [SNZ*21] extended the scope to magneto-viscoelastic materials by combining the material point method (MPM) with grid-based solvers for nonlinear magnetization.

Despite the remarkable progress in simulating the dynamics of both magnetic solids and fluids, the broader landscape of magnetic modeling and simulation for computer graphics remains fragmented and underexplored. The variety of approaches, ranging from magnetization models to force solvers, are all rooted in the same physical foundations, yet they have often been developed in isolation. Bringing these threads together is valuable not only for clarifying the underlying principles, but also for revealing commonalities that can inspire cross-fertilization between methods and applications. In this survey, we take a step toward this goal by consolidating existing advances into a coherent framework. We begin with the fundamental laws of magnetostatics (§2), then examine magneto-mechanical coupling (§3), summarizing its governing equations. Relying on these foundations, we review solvers for magnetic fields and magnetization (§4), as well as force evaluation and their integration into simulation systems (§5). Finally, in §6, we discuss the current landscape of capabilities and limitations, and highlight promising avenues for future research.

## 2. Magnetostatics

The magnetic phenomena of interest in computer graphics are typically those generated by magnetic fields induced by steady currents or permanent magnets, without the need to account for the effects of displacement currents (i.e., time-varying electric fields). In physics, magnetic fields that satisfy these conditions are well described by the theory of *magnetostatics*.

This section provides a brief overview of magnetostatics. For detailed derivations and explanations, we refer readers to the textbooks by Jackson [Jac98] or Griffiths [Gri23].

### 2.1. Fundamental Equations

For historical reasons, two vector fields, $\boldsymbol{B}$ and $\boldsymbol{H}$, are commonly used to describe magnetism. Although $\boldsymbol{B}$ is generally regarded as the more fundamental quantity, in the presence of material media (precisely the situations of interest in CG), $\boldsymbol{H}$ remains an important auxiliary field.

$\boldsymbol{B}$, we refer to as the *magnetic induction*, is derived from Ampère's molecular current hypothesis. This hypothesis asserts that free magnetic charges do not exist, implying that $\boldsymbol{B}$ is a field without sources and therefore divergence-free:

$$\nabla \cdot \boldsymbol{B} = 0, \tag{1}$$

which is known as *Gauss's law for magnetism*.

$\boldsymbol{H}$, we refer to as the *magnetic field*, is introduced by analogy with electric fields. In matter, the differential form of Ampère's circuit law relates $\boldsymbol{H}$ to the free current density $\boldsymbol{j}_\mathrm{f}$:

$$\nabla \times \boldsymbol{H} = \boldsymbol{j}_\mathrm{f}, \tag{2}$$

which can be simply called *Ampère's law*.

In vacuum, the magnetic induction is always proportional to the magnetic field, with the proportionality constant $\mu_0 = 4\pi \times 10^{-7}\,\mathrm{H\,m^{-1}}$, known as the *vacuum permeability*. In matter, however, the presence of an external magnetic field induces magnetization in the material, which in turn contribute to the magnetic induction. To quantify the magnetization, we introduce a vector field $\boldsymbol{M}$ that has the same physical dimension as $\boldsymbol{H}$. The constitutive relation among $\boldsymbol{B}$, $\boldsymbol{H}$, and $\boldsymbol{M}$ is expressed as

$$\boldsymbol{B} = \mu_0(\boldsymbol{H} + \boldsymbol{M}). \tag{3}$$

By construction, $\boldsymbol{M}$ vanishes identically outside the material.

Fundamentally, the magnetization $\boldsymbol{M}$, like the magnetic field $\boldsymbol{H}$, also originates from electric currents. The difference lies in the

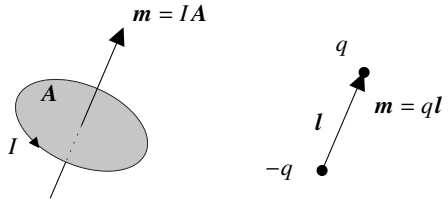


**Figure 2:** *The two equivalent definitions of a magnetic dipole. Left: the limiting case of a current loop; Right: the limiting case of a pair of opposite magnetic charges.*

source: $\boldsymbol{H}$ is generated by macroscopic free currents, but $\boldsymbol{M}$ is generated by so-called *bound currents* that arise from magnetized microscopic particles (see §2.3). Similar to Eq. (2), with the density of bound currents denoted $\boldsymbol{j}_\mathrm{b}$, the following relation holds:

$$\nabla \times \boldsymbol{M} = \boldsymbol{j}_\mathrm{b}. \tag{4}$$

By substituting Eq. (3) into the sum of Eqs. (2) and (4), we obtain

$$\nabla \times \boldsymbol{B} = \mu_0 \boldsymbol{j}, \tag{5}$$

where $\boldsymbol{j} = \boldsymbol{j}_\mathrm{f} + \boldsymbol{j}_\mathrm{b}$ is the total current density. This yields Ampère's law in vacuum.

**The Biot–Savart law.** Unlike Gauss's and Ampère's laws, which express the intrinsic properties of magnetic fields only implicitly, the Biot–Savart law provides an explicit formula for the magnetic induction generated by a current distribution:

$$\boldsymbol{B}(\boldsymbol{x}) = \frac{\mu_0}{4\pi} \iiint_{V'} \frac{\boldsymbol{j}(\boldsymbol{x}') \times (\boldsymbol{x} - \boldsymbol{x}')}{\|\boldsymbol{x} - \boldsymbol{x}'\|^3} \mathrm{d}V'. \tag{6}$$

In essence, this expression can be regarded as the Green's function solution to Eqs. (1) and (5), subject to boundary conditions at infinity.

## 2.2. Magnetic Dipoles

Since no isolated positive or negative magnetic charges (i.e., magnetic monopoles) have ever been observed, the dipole constitutes the leading term in the multipole expansion of the magnetic induction. From the perspective of either $\boldsymbol{B}$ or $\boldsymbol{H}$ , a magnetic dipole can be defined in two equivalent ways:

(1) as the limiting case of a current loop carrying current $I$ and enclosing an area $\boldsymbol{A}$, with $I\boldsymbol{A}$ held fixed as $A \to 0$; or
(2) as the limiting case of a pair of opposite magnetic charges $\pm q$ separated by a distance $l$, with $q\boldsymbol{l}$ held fixed as $l \to 0$.

The *magnetic dipole moment* (often abbreviated as the *magnetic moment*) $\boldsymbol{m}$ is defined to have a magnitude of either $I\boldsymbol{A}$ or $q\boldsymbol{l}$, and a direction given either by the loop's normal according to the right-hand rule or from the negative toward the positive magnetic charge. Fig. 2 illustrates the two definitions of a magnetic dipole.

The magnetic dipole model plays a central role in understanding magnetization and modeling permanent magnets. Based on the current-loop definition, we can use the Biot–Savart law to show that a magnetic moment $\boldsymbol{m}$ generates the magnetic induction

$$\boldsymbol{B}(\boldsymbol{x}) = \frac{\mu_0}{4\pi} \frac{3\hat{\boldsymbol{r}}(\boldsymbol{m} \cdot \hat{\boldsymbol{r}}) - \boldsymbol{m}}{\|\boldsymbol{r}\|^3} + \frac{2\mu_0}{3} \boldsymbol{m}\, \delta(\boldsymbol{r}), \tag{7}$$

where $\boldsymbol{r} = \boldsymbol{x} - \boldsymbol{x}_0$, $\hat{\boldsymbol{r}} = \boldsymbol{r}/\|\boldsymbol{r}\|$, $\boldsymbol{x}_0$ denotes the dipole position, and $\delta(\boldsymbol{r})$ is the three-dimensional Dirac delta function. Alternatively, starting from the magnetic-charge definition and Coulomb's law, the magnetic field produced by this moment can be derived as

$$\boldsymbol{H}(\boldsymbol{x}) = \frac{1}{4\pi} \frac{3\hat{\boldsymbol{r}}(\boldsymbol{m} \cdot \hat{\boldsymbol{r}}) - \boldsymbol{m}}{\|\boldsymbol{r}\|^3} - \frac{1}{3} \boldsymbol{m}\, \delta(\boldsymbol{r}). \tag{8}$$

By dividing Eq. (7) by $\mu_0$ and subtracting Eq. (8), we obtain

$$\boldsymbol{M}(\boldsymbol{x}) = \boldsymbol{m}\, \delta(\boldsymbol{r}), \tag{9}$$

which once again demonstrates that the magnetization serves as a bridge between the two perspectives on magnetism.

## 2.3. Magnetization and Magnetism

Ampère's molecular current hypothesis proposes that each fundamental unit of a magnetic material—namely, a molecule (or, as we now know, possibly an atom or ion)—contains an internal loop current. In other words, each unit can be considered a magnetic dipole. Accordingly, based on Eq. (9) and the principle of superposition, the magnetization within a material can be defined as

$$\boldsymbol{M}(\boldsymbol{x}) = \lim_{\Delta V \to 0} \frac{\sum_i \boldsymbol{m}_i}{\Delta V}, \tag{10}$$

which sums over all magnetic moments within an infinitesimal volume $\Delta V$ surrounding the point $\boldsymbol{x}$. The hypothesis further states that the magnitude of the magnetic moment carried by identical molecules is invariant, while its orientation may vary depending on the molecular alignment. In most cases, the orientations of these magnetic moments are random, resulting in $\boldsymbol{M} = \boldsymbol{0}$, and the magnetic fields produced by individual units cancel each other, so the material exhibits no macroscopic magnetism. However, when an external magnetic field is applied, the magnetic moments tend to align along the field direction, giving rise to a nonzero magnetization, $\boldsymbol{M} \neq \boldsymbol{0}$, which manifests macroscopically as the material becoming magnetized.

### 2.3.1. Magnetism in Common Materials

Variations in how molecular magnetic moments respond to external fields lead to distinct types of magnetism in materials. The most common categories are diamagnetism, paramagnetism, and ferromagnetism.

**Diamagnetism.** All materials exhibit diamagnetism, an effect arising from electromagnetic induction in atomic electrons that produces a response opposing an external magnetic field. The magnitude of diamagnetism is typically very small, and in most substances it is masked by other forms of magnetism. According to Langevin's classical theory [Lan05], the magnetization induced by this effect is always antiparallel to $\boldsymbol{H}$ and can be calculated as

$$\boldsymbol{M} = -\frac{n\mu_0 \mathrm{e}^2 Z \overline{a^2}}{6m} \boldsymbol{H}, \tag{11}$$

where $\mathrm{e} \approx 1.602 \times 10^{-19}\,\mathrm{C}$ is the elementary charge, $Z$ is the number of orbital electrons per atom, $m$ is the electron mass, $\overline{a^2}$ denotes the mean square radius of the electron orbit, and $n$ is the number density of atoms in the material. For substances containing multiple atomic species, the total magnetization should be obtained by evaluating Eq. (11) for each species and summing the contributions.

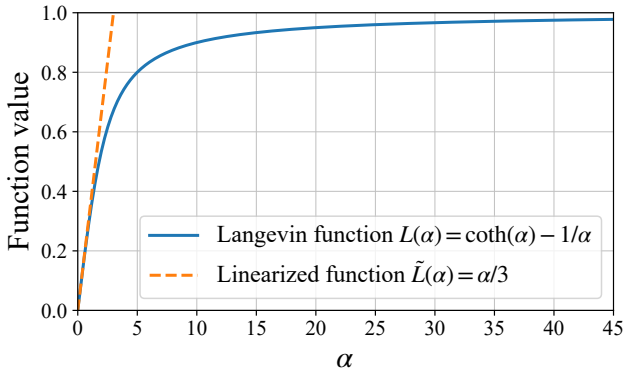


**Figure 3:** *Plot of the Langevin function. For small $\alpha$, the growth is nearly linear, while for large $\alpha$, the function approaches* 1 *asymptotically without ever reaching it.*

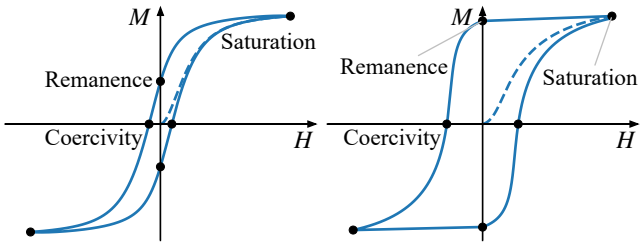


**(a)** *Soft magnetic materials;* **(b)** *Hard magnetic materials.*

**Figure 4:** *Hysteresis loops of ferromagnetic materials in one dimension. Initially, the magnetization M increases with the applied field H until saturation. As H decreases back to zero, M remains nonzero, exhibiting remanence. Demagnetization requires reversing H to a certain magnitude, known as the* coercivity.

**Paramagnetism.** Paramagnetism refers to the property of materials that exhibit a weak positive response to an external magnetic field. Substances exhibiting paramagnetism are widespread, including alkali metals and all transition elements except iron, cobalt, and nickel. Based on thermodynamics and statistical physics, Langevin's classical theory [Lan05] derives the following expression for the magnetization of paramagnetic materials:

$$\boldsymbol{M} = nm\,L\left(\frac{\mu_0 m\|\boldsymbol{H}\|}{k_{\mathrm{B}}T}\right)\frac{\boldsymbol{H}}{\|\boldsymbol{H}\|}, \tag{12}$$

where $k_{\mathrm{B}} \approx 1.381\times10^{-23}\,\mathrm{J\,K^{-1}}$ is the Boltzmann constant, $T$ is the absolute temperature, $m$ is the magnitude of each magnetic moment, and $n$ is the moments' number density. The function $L(\cdot)$ in Eq. (12), known as the Langevin function, is defined as

$$L(\alpha) = \coth\alpha - \frac{1}{\alpha}, \tag{13}$$

which approaches 1 as $\alpha \to \infty$, thereby bounding the maximum possible magnetization. See Fig. 3 for illustration.

**Ferromagnetism.** Unlike diamagnetism or paramagnetism, ferromagnetic materials (such as iron, cobalt, and nickel) exhibit a strong response to external magnetic fields. As the field strength $\boldsymbol{H}$ increases, the magnetization $\boldsymbol{M}$ rises rapidly until it reaches saturation. When $\boldsymbol{H}$ is subsequently reduced, the decrease in $\boldsymbol{M}$ is smaller than its previous increase. Remarkably, even after the external field is completely removed, a ferromagnet can retain a nonzero *remanent magnetization* in the original direction of $\boldsymbol{H}$. This behavior is referred to as *hysteresis*. Fig. 4 illustrates the hysteresis loops of two types of ferromagnetism that correspond to so-called soft and hard magnetic materials:

- Soft magnetic materials exhibit narrow hysteresis loops with small remanent magnetization;
- Hard magnetic materials exhibit wide hysteresis loops, with magnetization that remains nearly unchanged upon removal of the external field.

Consequently, hard magnetic materials are widely used in the fabrication of permanent magnets. By contrast, hysteresis leads to a magnetic response that depends on the magnetization path. The resulting effective anisotropy means that the magnetization $\boldsymbol{M}$ is generally not aligned with the applied field $\boldsymbol{H}$.

### 2.3.2. Quantification and Linearization

To quantify and compare the strength of magnetic responses across materials, when the magnetization and magnetic field are aligned, the ratio of $\boldsymbol{M}$ to $\boldsymbol{H}$ is commonly defined in engineering and physics as the *magnetic susceptibility*, denoted by $\chi$:

$$\boldsymbol{M} = \chi\boldsymbol{H}, \qquad \text{for a given material.} \tag{14}$$

In general, for pure substances, the susceptibility of diamagnetic materials is on the order of $-10^{-5}$ to $-10^{-6}$, that of paramagnetic materials ranges from $10^{-5}$ to $10^{-3}$, and that of ferromagnetic materials exceeds 10, reaching values as high as $10^5$.

Substituting Eq. (14) into Eq. (3) yields

$$\boldsymbol{B} = \mu_{\mathrm{r}}\mu_0\boldsymbol{H} = \mu\boldsymbol{H}, \qquad \text{for a given material,} \tag{15}$$

where $\mu_{\mathrm{r}} = 1+\chi$ is the *relative permeability*, and $\mu = \mu_{\mathrm{r}}\mu_0$ is the *permeability*. With these parameters, magnetization can be regarded as a correction to the vacuum constitutive relation $\boldsymbol{B} = \mu_0\boldsymbol{H}$.

In practice, even for a given material, the susceptibility $\chi$ and permeability $\mu$ are not constant, as they depend on the magnetic field strength and hysteresis effects. Nevertheless, in many cases these parameters can be approximated as constants, allowing the material to be treated as linearly magnetizable. Specifically:

- According to Eq. (11), the ratio $\boldsymbol{M}/\boldsymbol{H}$ for diamagnetism is independent of the external field, so the magnetization of diamagnetic materials are typically regarded as linear.
- From the Taylor expansion of the Langevin function defined in Eq. (13) at $\alpha = 0$, namely $L(\alpha) = \alpha/3 + O(\alpha^3)$, it follows that paramagnetism can be linearized under weak-field conditions.
- For soft magnetic materials, the hysteresis loop approximately passes through the origin, and its slope can be taken as the susceptibility under weak fields.

## 2.4. Magnetic Forces

A charged particle moving in a magnetic field experiences a Lorentz force that is perpendicular to both its velocity and the di-

rection of the magnetic induction. Expressed in terms of current density, the force density is

$$\boldsymbol{f} = \boldsymbol{j} \times \boldsymbol{B}. \tag{16}$$

Applying this expression to the current-loop definition of a magnetic dipole, one can show that a magnetic moment $\boldsymbol{m}$ in a magnetic field experiences a torque that tends to align it with $\boldsymbol{B}$:

$$\boldsymbol{\tau} = \boldsymbol{m} \times \boldsymbol{B}. \tag{17}$$

Similarly, the force on $\boldsymbol{m}$ due to a nonuniform magnetic field can be expressed as

$$\boldsymbol{F} = (\boldsymbol{m} \times \boldsymbol{\nabla}) \times \boldsymbol{B} = \boldsymbol{\nabla}(\boldsymbol{m} \cdot \boldsymbol{B}), \tag{18}$$

where $\boldsymbol{m}$ is treated as constant when taking spatial derivatives. This allows us to define the potential energy of a magnetic moment in a magnetic field as

$$W = -\boldsymbol{m} \cdot \boldsymbol{B}. \tag{19}$$

Computing the torque and force on a magnetic dipole is relatively straightforward, but evaluating the force exerted on a bulk magnetic medium is considerably more involved. Similar to continuum mechanics, electrodynamics introduces the *Maxwell stress tensor* $\boldsymbol{T}$, which allows the magnetic force density to be expressed as the divergence of $\boldsymbol{T}$:

$$\boldsymbol{f} = \boldsymbol{\nabla} \cdot \boldsymbol{T}. \tag{20}$$

The derivation of $\boldsymbol{T}$ generally starts from the Lorentz force law (Eq. (16)). However, in matter, different treatments of the electromagnetic work lead to ambiguity regarding the appropriate form of $\boldsymbol{T}$. This issue gave rise to the well-known *Abraham–Minkowski controversy* in the late 19th and early 20th centuries.

Considering the magnetic part of $\boldsymbol{T}$, the *Einstein–Laub formulation* [EL08] asserts that

$$\boldsymbol{T}_{\text{Ein}} = \boldsymbol{B} \otimes \boldsymbol{H} - \frac{\mu_0}{2} \|H\|^2 \boldsymbol{I}, \tag{21}$$

where $\boldsymbol{I}$ is the identity tensor. From this, we can obtain the magnetic force density

$$\boldsymbol{f}_{\text{Kel}} = \boldsymbol{\nabla} \cdot \boldsymbol{T}_{\text{Ein}} = \mu_0 (\boldsymbol{M} \cdot \boldsymbol{\nabla}) \boldsymbol{H}, \tag{22}$$

commonly referred to as the *Kelvin force*. By contrast, the *Minkowski formulation* [Min08] proposes

$$\boldsymbol{T}_{\text{Min}} = \boldsymbol{B} \otimes \boldsymbol{H} - \frac{1}{2} (\boldsymbol{B} \cdot \boldsymbol{H}) \boldsymbol{I}, \tag{23}$$

which leads to the force density

$$\boldsymbol{f}_{\text{Min}} = \boldsymbol{\nabla} \cdot \boldsymbol{T}_{\text{Min}} = (\boldsymbol{B} \cdot \boldsymbol{\nabla}) \boldsymbol{H} - \frac{1}{2} \boldsymbol{\nabla} (\boldsymbol{B} \cdot \boldsymbol{H}). \tag{24}$$

For an isotropic linear magnetization, Eqs. (22) and (24) reduce to

$$\boldsymbol{f}_{\text{Kel}} = \frac{\mu_0}{2} \chi \boldsymbol{\nabla} \left( \|\boldsymbol{H}\|^2 \right), \tag{25}$$

$$\boldsymbol{f}_{\text{Hel}} = -\frac{\mu_0}{2} \|\boldsymbol{H}\|^2 \boldsymbol{\nabla} \chi, \tag{26}$$

where the latter is known as the *Helmholtz force*.

It should be noted that, despite their different mathematical forms, all expressions for the magnetic force density are experimentally valid [AFM*22]. The apparent discrepancy among these formulations originates from different conventions in partitioning stresses between the electromagnetic field and the mechanical medium. The linear results in Eqs. (25) and (26) provide a particularly transparent illustration of this freedom: the difference between force densities derived from alternative Maxwell stress tensors can be expressed as the gradient of a scalar field, which can be absorbed into the mechanical stress without affecting observable quantities.

Moreover, since $\boldsymbol{B}$, $\boldsymbol{H}$, and $\boldsymbol{M}$ may undergo discontinuities across material interfaces, the interfacial magnetic force corresponds to the net pressure given by the jump in $\boldsymbol{T} \cdot \boldsymbol{n}$ between the two media, where $\boldsymbol{n}$ denotes the unit normal to the interface. Consequently, when all materials involved are linearly magnetizable and are separated by well-defined interfaces, the Helmholtz force model is almost always the most convenient—and often the optimal—choice. In this case, the magnetic force is entirely concentrated at material boundaries in the form of surface tractions, while no magnetic body force arises within the bulk.

## 3. Magneto-Mechanical Coupling

Having reviewed the principles of magnetostatics, we now incorporate the effects of magnetic fields into mechanical analysis through the concepts of magnetic forces. In this section, we continue to work from a continuous perspective, under which we mathematically model magneto-mechanical coupling and derive the governing equations for simulating the dynamics of magnetic materials.

### 3.1. Determination of Magnetic Fields

As discussed in §2.4, magnetic forces are always functions of the field vectors (i.e., $\boldsymbol{B}$, $\boldsymbol{H}$, and $\boldsymbol{M}$). Therefore, the calculation of magnetic forces requires the prior computations of the magnetic fields themselves. Under the quasistatic assumption of magnetostatics, both the relaxation time of field variations and electromagnetic induction effects can be neglected. Consequently, whenever the configuration of magnetic materials changes, the field instantaneously relaxes to a new equilibrium consistent with the prescribed boundary conditions. In other words, magnetic fields can always be *determined* directly from the current material distribution, rather than *evolved* from their past history.

In general, the systems we simulate are not isolated and may be subject to magnetic fields generated by external permanent magnets or steady currents. Denoting these prescribed external contributions by $\boldsymbol{B}_{\text{ext}}$ and $\boldsymbol{H}_{\text{ext}}$, and the fields induced by the internal material magnetization by $\boldsymbol{B}_{\text{int}}$ and $\boldsymbol{H}_{\text{int}}$, the total fields are written as

$$\begin{cases} \boldsymbol{B} = \boldsymbol{B}_{\text{ext}} + \boldsymbol{B}_{\text{int}}, & \text{(27a)} \\ \boldsymbol{H} = \boldsymbol{H}_{\text{ext}} + \boldsymbol{H}_{\text{int}}. & \text{(27b)} \end{cases}$$

The external fields themselves satisfy Gauss's law, Ampère's law, and the constitutive relation in the simulation domain:

$$\begin{cases} \boldsymbol{\nabla} \cdot \boldsymbol{B}_{\text{ext}} = 0, & \text{(28a)} \\ \boldsymbol{\nabla} \times \boldsymbol{H}_{\text{ext}} = \boldsymbol{0}, & \text{(28b)} \\ \boldsymbol{B}_{\text{ext}} = \mu_0 \boldsymbol{H}_{\text{ext}}, & \text{(28c)} \end{cases}$$

with the free currents producing $\boldsymbol{H}_{\text{ext}}$ assumed to lie outside the system and thus neglected. Fig. 5 illustrates such a decomposition of the magnetic field.

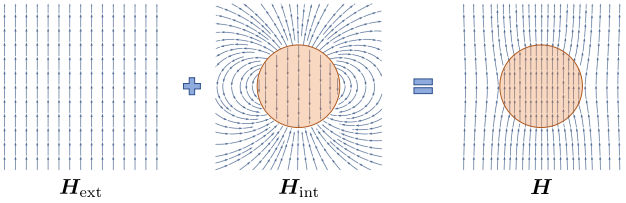


**Figure 5:** *A sphere in a uniform magnetic field ($\boldsymbol{H}_{\text{ext}}$) is magnetized and produces an induced field ($\boldsymbol{H}_{\text{int}}$), which further leads to a synthesized field ($\boldsymbol{H}$) as their summation. Source: Ni et al. [NZWC20].*

The internal magnetic fields $\boldsymbol{B}_{\text{int}}$ and $\boldsymbol{H}_{\text{int}}$ are the unknowns to be solved. Subtracting Eq. (28b) from Eq. (2), we readily see that, for systems without internal free currents ($\boldsymbol{j}_{\text{f}} = \boldsymbol{0}$, which is the case for scenarios of interest in CG), $\boldsymbol{H}_{\text{int}}$ is irrotational:

$$\nabla \times \boldsymbol{H}_{\text{int}} = \boldsymbol{0}, \tag{29}$$

allowing the introduction of a scalar potential $\phi$ such that $\boldsymbol{H}_{\text{int}} = -\nabla\phi$. Substituting this into Eqs. (1), (3), (27), and (28) yields the governing scalar equation

$$\nabla^2\phi = \nabla \cdot \boldsymbol{M}(\boldsymbol{H}), \tag{30}$$

where $\boldsymbol{M}$ is typically modeled as a function only of the local field $\boldsymbol{H} = \boldsymbol{H}_{\text{ext}} - \nabla\phi$ (ferromagnetic materials with pronounced hysteresis being a notable exception). In this formulation, $\phi$ is the sole independent unknown, uniquely determined by imposing the boundary condition at infinity:

$$\phi(\boldsymbol{x}) \to 0 \quad \text{as} \quad \|\boldsymbol{x}\| \to \infty. \tag{31}$$

### 3.2. Equations of Motion for Magnetic Materials

Overall, the equations of motion for magnetic materials can be regarded as those for their non-magnetic counterparts, with the addition of a magnetic force term. To keep this survey self-contained, we present the governing equations for different classes of materials according to their kinematic form.

In the following text, we denote by $\boldsymbol{g}$ the gravitational acceleration, by $\boldsymbol{f}$ the original external force density term, and by $\boldsymbol{f}_{\text{m}}$ the additional magnetic body-force density.

#### 3.2.1. Magnetic Rigid Bodies

The motion of a rigid body follows Newton's second law for linear momentum and Euler's equation for angular momentum:

$$\begin{cases} M\dot{\boldsymbol{v}} = M\boldsymbol{g} + \iiint_V (\boldsymbol{f} + \boldsymbol{f}_m)\,\mathrm{d}V, & \text{(32a)} \\ \boldsymbol{I}\dot{\boldsymbol{\omega}} + \boldsymbol{\omega} \times (\boldsymbol{I}\boldsymbol{\omega}) = \iiint_V (\boldsymbol{x} - \boldsymbol{x}_{\text{c}}) \times (\boldsymbol{f} + \boldsymbol{f}_m)\,\mathrm{d}V, & \text{(32b)} \end{cases}$$

where $\boldsymbol{v}$ is the translational velocity of the center of mass $\boldsymbol{x}_{\text{c}}$, $\boldsymbol{\omega}$ is the angular velocity, $M$ is the total mass of the body $V$, and $\boldsymbol{I}$ is the inertia tensor about the center of mass.

#### 3.2.2. Magnetic Deformable Continua

Unlike rigid bodies, the internal forces in deformable continua (including primarily elastic solids and fluids) cannot be prescribed arbitrarily but must be represented through the divergence of the Cauchy stress tensor $\boldsymbol{\sigma}$. The equations of motion for magnetic deformable continua are therefore governed by the so-called *Cauchy momentum equation*:

$$\rho\left[\frac{\partial \boldsymbol{u}}{\partial t} + (\boldsymbol{u} \cdot \nabla)\boldsymbol{u}\right] = \nabla \cdot \boldsymbol{\sigma} + \rho\boldsymbol{g} + \boldsymbol{f} + \boldsymbol{f}_{\text{m}}, \tag{33}$$

where $\rho$ denotes the mass density and $\boldsymbol{u}$ the velocity field. The specific constitutive form of the Cauchy stress tensor $\boldsymbol{\sigma}$ characterizes the material behavior of the continuum.

**Elastic solids.** Depending on the choice of hyperelastic model, there are multiple ways to define the Cauchy stress tensor for elastic solids [SB12]. One widely used model that offers both accuracy and numerical stability for volumetric elastomer simulations is the *Neo-Hookean constitutive model*:

$$\boldsymbol{\sigma} = \frac{\mu}{J}\left(\boldsymbol{F}\boldsymbol{F}^{\top} - \boldsymbol{I}\right) + \frac{\lambda \log J}{J}\boldsymbol{I}, \tag{34}$$

where $\mu$ and $\lambda$ are the first and second Lamé parameters, $\boldsymbol{I}$ denotes the identity tensor, $\boldsymbol{F}$ is the deformation gradient, and $J = |\boldsymbol{F}|$ represents the volumetric change. For thin-shell elastomers, a common choice is the *St. Venant–Kirchhoff (StVK) model*, expressed as

$$\boldsymbol{\sigma} = \frac{\mu}{J}\boldsymbol{F}\left(\boldsymbol{F}^{\top}\boldsymbol{F} - \boldsymbol{I}\right)\boldsymbol{F}^{\top} + \frac{\lambda\,\mathrm{tr}\left(\boldsymbol{F}^{\top}\boldsymbol{F} - \boldsymbol{I}\right)}{2J}\boldsymbol{F}\boldsymbol{F}^{\top}. \tag{35}$$

Integrating the momentum equation (33) through the shell thickness yields a surficial formulation [Wei12], suitable for shell simulations, rather than a fully volumetric one.

**Incompressible fluids.** For incompressible fluids, the Cauchy stress tensor is typically described by *Stokes's constitutive relation*, which decomposes the stress into volumetric (pressure) and deviatoric (viscosity) components [Bat00]:

$$\boldsymbol{\sigma} = -p\boldsymbol{I} + \nabla \cdot \mu\left[\nabla\boldsymbol{u} + (\nabla\boldsymbol{u})^{\top}\right], \tag{36}$$

Here, $p$ denotes the pressure and $\mu$ the dynamic viscosity (analogous to the first Lamé parameter in solids). Substituting Eq. (36) into Eq. (33) yields the *incompressible Navier–Stokes equations*, which must be solved together with the incompressibility constraint $\nabla \cdot \boldsymbol{u} = 0$ to determine $p$. A typical representative of incompressible fluids is liquid. Liquids possess a well-defined free surface, across which surface tension arises. This effect is commonly expressed as a pressure difference

$$\Delta p = 2\gamma\kappa, \tag{37}$$

where $\gamma$ denotes the surface tension coefficient and $\kappa$ is the mean curvature of the surface. Besides, if the assumption of an ideal fluid supporting arbitrary positive pressures is relaxed, the isotropic stress term $-p\boldsymbol{I}$ should be replaced with a hyperelastic stress formulation (e.g., Eq. (34)). This modification leads to the governing equations for (nearly) incompressible viscoelastic fluids [RGJ*15].

## 4. Magnetostatic Solvers

Building on the governing equations introduced in §3.1 and §3.2, incorporating magnetic effects into numerical algorithms requires augmenting traditional physical simulation pipelines in two complementary aspects:

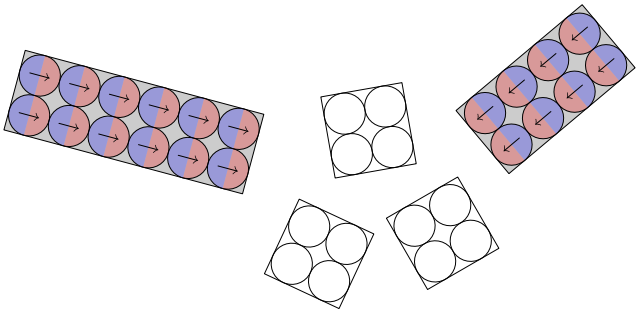

**Figure 6:** *Magnetic rigid bodies are decomposed into cells, each with a magnetic dipole located at its center. The dipoles inside soft ferromagnetic objects (colored) are polarized by the magnetic field. Source: Westhofen et al. [WFJB24].*

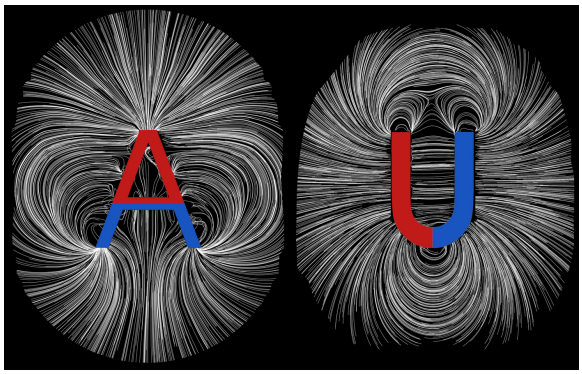

**Figure 7:** *The direct magnetization method can be used to compute magnetic field lines. "North" and "south" poles of the magnets are shown in red and blue. Source: Thomaszewski et al. [TGPS08].*

(1) A dedicated stage of magnetostatic solvers that model material magnetization and compute the system's magnetic fields; and
(2) The evaluation of magnetic forces on objects and their integration into existing time-stepping schemes.

In this section, we present a systematic categorization of magnetostatic solvers in the computer graphics literature, while deferring the discussion of force application to §5.

### 4.1. Dipole-Based Approaches

Solving the governing equations of magnetostatics (§3.1) is generally complex and computationally expensive, making real-time simulation challenging. Fortunately, for rigid bodies, whose internal magnetic interactions can be safely neglected, it is often unnecessary to compute a continuous magnetization field. Instead, the body's magnetic behavior can be efficiently approximated using one or several discrete magnetic dipole moments, providing a compact yet effective representation of its magnetization.

#### 4.1.1. Direct Magnetization Methods

Thomaszewski et al. [TGPS08] discretized a rigid body into a collection of small cells, each represented by a magnetic dipole $\boldsymbol{m}_i$ located at its center $\boldsymbol{x}_i$ (Fig. 6). For permanent magnets, these dipoles are predefined and rigidly attached to the material, translating and rotating with the body as a whole. When determining the magnetic field, the external magnetic induction $\boldsymbol{B}_{\text{ext}}$ can be obtained by summing the contributions of all such dipoles:

$$\boldsymbol{B}_{\text{ext}}(\boldsymbol{x}) = \frac{\mu_0}{4\pi} \sum_{i \in P} \frac{3(\boldsymbol{x}-\boldsymbol{x}_i)\left[\boldsymbol{m}_i \cdot (\boldsymbol{x}-\boldsymbol{x}_i)\right] - \|\boldsymbol{x}-\boldsymbol{x}_i\|^2 \boldsymbol{m}_i}{\|\boldsymbol{x}-\boldsymbol{x}_i\|^5}, \quad (38)$$

where $P$ denotes the index set of cells belonging to the permanent magnets. The above expression directly follows from Eq. (7).

For other magnetically responsive rigid bodies, assumed to exhibit linear magnetization, we denote their cell indices by $Q$. Each cell is assumed to be spherical, and because of its small size, the magnetic induction inside can be regarded as uniform. Under this assumption, the magnetization within a cell is homogeneous, leading to the analytical form

$$\boldsymbol{M}_i = \frac{1}{\mu_0} \frac{3\chi}{3+\chi} \left[\boldsymbol{B}_{\text{ext}}(\boldsymbol{x}_i) + \boldsymbol{B}^*_{\text{int}}(\boldsymbol{x}_i)\right], \quad (39)$$

where $\boldsymbol{B}^*_{\text{int}}$ is $\boldsymbol{B}_{\text{int}}$ excluding the self-induced field of $\boldsymbol{m}_i$. Considering that $\boldsymbol{M}$ represents the magnetic moment density (see Eq. (10)), similar to Eq. (38), we can expand $\boldsymbol{B}^*_{\text{int}}$ to yield the following expression for each $\boldsymbol{m}_i$:

$$\boldsymbol{m}_i = \frac{V_i}{\mu_0} \frac{3\chi}{3+\chi} \left[\boldsymbol{B}_{\text{ext}}(\boldsymbol{x}_i) + \frac{\mu_0}{4\pi} \sum_{j \in Q, j \neq i} \frac{3\hat{\boldsymbol{r}}_j(\boldsymbol{m}_j \cdot \hat{\boldsymbol{r}}_j) - \boldsymbol{m}_j}{\|\boldsymbol{r}_j\|^3}\right], \quad (40)$$

where $\boldsymbol{r}_j = \boldsymbol{x} - \boldsymbol{x}_j$, $\hat{\boldsymbol{r}}_j = \boldsymbol{r}_j / \|\boldsymbol{r}_j\|$, and $V_i$ denotes the volume of the $i$-th cell.

Eq. (40) indicates that both sides depend on the unknown dipole moments $\{\boldsymbol{m}_i\}$, requiring either an iterative procedure or the solution of a global linear system. For stability and convergence considerations, however, Thomaszewski et al. [TGPS08] simplified the formulation by retaining only the external field $\boldsymbol{B}_{\text{ext}}$ on the right-hand side, thereby neglecting the contribution of the induced internal field $\boldsymbol{B}^*_{\text{int}}$. To better account for the neglected mutual induction, Westhofen et al. [WFJB24] later proposed an improvement in which the induced term (i.e., the summation over linearly magnetized cells) uses the dipole moments $\boldsymbol{m}_j$ from the previous time step as an approximation. This strategy enhances physical accuracy while incurring almost no additional computational cost, providing a balanced compromise between efficiency and realism.

The magnetic field lines generated using the direct magnetization method are plotted as shown in Fig. 7.

**Hard-magnetic soft bodies.** As mentioned earlier, the magnetic moments $\boldsymbol{m}_i$ of permanent magnets are predetermined and simply undergo rigid translation and rotation with the body as a whole, without requiring additional computation. This concept can be extended to deformable solids with continuous magnetization fields. For hard-magnetic soft bodies, Chen et al. [CNZ*22] assumed that the magnetization in the material (reference) space, denoted $\overline{\boldsymbol{M}}$, is prescribed in advance. During deformation, the spatial magnetiza-

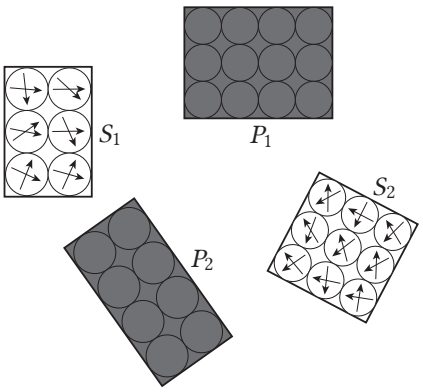


**Figure 8:** *Magnetic rigid bodies are decomposed into cells, each with two magnetic dipoles (or equivalently, submagnetizations). Permanent magnets ($P_1$ and $P_2$) are shaded since it cannot be polarized by the magnetic field. Source: Kim et al. [KPH18].*

tion can be computed as

$$\boldsymbol{M} = J^{-1}\boldsymbol{F}\overline{\boldsymbol{M}}, \tag{41}$$

In systems composed purely of hard-magnetic materials, once $\boldsymbol{M}$ is calculated, the corresponding fields $\boldsymbol{H}$ and $\boldsymbol{B}$ follow directly, completing the determination of the magnetic field.

#### 4.1.2. Magnetization Dynamics Methods

To accurately capture mutual induction and nonlinear magnetization, Kim et al. [KPH18] drew inspiration from micromagnetics and formulated the magnetization dynamics between discrete magnetic moments at the macroscopic scale. As Thomaszewski et al. [TGPS08], each rigid body is discretized into a set of cells. However, instead of placing a single dipole in each cell, Kim et al. [KPH18] introduced two normalized dipoles, $\boldsymbol{m}_i^1$ and $\boldsymbol{m}_i^2$, at the cell center (Fig. 8). These dipoles are constrained to have constant magnitude and evolve under the influence of the magnetic field according to the *Landau–Lifshitz–Gilbert (LLG) equation*:

$$\frac{\mathrm{d}\boldsymbol{M}_i^p}{\mathrm{d}t} = -\frac{\gamma}{1+\alpha^2}\boldsymbol{M}_i^p \times \left(\boldsymbol{H} + \alpha \boldsymbol{M}_i^p \times \boldsymbol{H}\right), \tag{42}$$

where $\boldsymbol{M}_i^p = \boldsymbol{m}_i^p / V_i$ denotes the submagnetization, $\gamma$ is the gyromagnetic ratio, and $\alpha$ is a material-specific damping constant. The overall magnetization of each cell is given by the average of its two submagnetizations, i.e., $\boldsymbol{M}_i = (\boldsymbol{M}_i^1 + \boldsymbol{M}_i^2)/2$. Assuming again that each cell is spherical, the magnetic field $\boldsymbol{H}$ in the LLG equation can be expressed as

$$\boldsymbol{H}(\boldsymbol{x}_i) = \boldsymbol{H}^*(\boldsymbol{x}_i) - \frac{1}{3}\boldsymbol{M}_i, \tag{43}$$

where $\boldsymbol{H}^* = \boldsymbol{H}_{\text{ext}} + \boldsymbol{B}^*_{\text{int}}/\mu_0$. Note that we denote the field simply as $\boldsymbol{H}$ instead of $\boldsymbol{H}_{\text{eff}}$ as in the original paper, since at the macroscopic scale of interest, unlike in micromagnetics, the demagnetizing field is implicitly included in $\boldsymbol{H}$.

To determine the magnetic field for a given material setup, we can integrate the virtual time-stepping form of Eq. (42) until a steady state is reached. Kim et al. [KPH18] adopted a semi-implicit integration scheme originally proposed by Serpico et al. [SMB01]. This method combines the midpoint rule with an appropriate extrapolation formula, which guarantees the preservation of magnetization magnitude throughout the integration process.

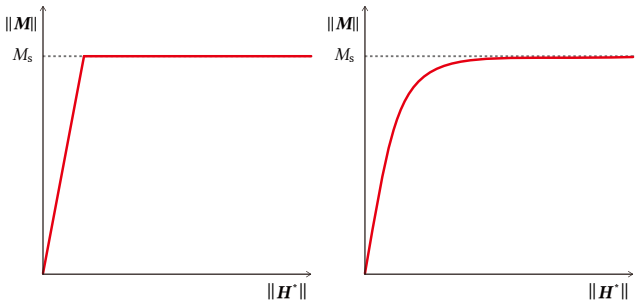


**(a)** *Non-differentiable [KPH18];* **(b)** *Differentiable [KH22].*

**Figure 9:** *Magnetization curves of the magnetization dynamics methods. Source: Kim and Han [KH22].*

**Remanence.** Using magnetization dynamics methods, we can qualitatively reproduce the remanent magnetization behavior observed in ferromagnetic materials. The *magnetocrystalline anisotropy* defines a set of easy axes within a ferromagnet. When the magnetization direction $\boldsymbol{M}_i$ deviates from all of these easy axes, an additional field term $\boldsymbol{H}_{\text{K}}$ arises in $\boldsymbol{H}$, which drives $\boldsymbol{M}_i$ to realign toward the nearest easy axis. This mechanism can be easily incorporated into the time integration of the LLG equation with respect to $\boldsymbol{M}_i^p$, simply by modifying the evaluation of the effective magnetic field $\boldsymbol{H}$ at each virtual time step.

**Susceptibility.** In magnetization dynamics methods, the resulting magnetization curve is inherently nonlinear, since the magnitudes of $\boldsymbol{m}_i^1$ and $\boldsymbol{m}_i^2$ are constant. Even when these vectors align, they can only produce a magnetization of limited magnitude. From Eq. (42), it can be observed that at steady state, either $\boldsymbol{H} \neq \boldsymbol{0}$ and $\boldsymbol{M}_i^p \parallel \boldsymbol{H}$, or $\boldsymbol{H} = \boldsymbol{0}$. The former corresponds to the saturated magnetization condition, whereas the latter implies that the concept of magnetic susceptibility with respect to $\boldsymbol{H}$ loses its meaning. Nevertheless, we can define a modified susceptibility $\chi^*$ as the ratio between $\boldsymbol{M}$ and the modified field $\boldsymbol{H}^*$. From Eq. (43), it follows that $\chi^* = 3$. This motivates replacing the constant coefficient $1/3$ in the formulation with an adjustable self-demagnetizing factor $\gamma_{\text{D}}$, thereby relaxing the assumption of spherical cells [KH20]. Effectively, $\gamma_{\text{D}}$ determines how $\boldsymbol{B}$ relates to $\boldsymbol{M}$ as

$$\frac{1}{\mu_0}\boldsymbol{B} = \frac{1}{\gamma_{\text{D}}}\boldsymbol{M}, \tag{44}$$

under which the modified susceptibility becomes $\chi^* = 1/\gamma_{\text{D}}$.

**Stability Enhancements.** The original LLG equation (42) contains a precession term $\boldsymbol{M}_i^p \times \boldsymbol{H}$ that deteriorates the convergence efficiency. To address this issue, Kim and Han [KH22] neglected this term and retained only the damping term $\boldsymbol{M}_i^p \times \left(\boldsymbol{M}_i^p \times \boldsymbol{H}\right)$. Since the magnitude of the magnetization $\|\boldsymbol{M}_i^p\|$ is a constant in LLG equation, the evolution can be described by the angle $\theta_i^p$ be-

tween $\boldsymbol{M}_i^p$ and $\boldsymbol{H}$. Taking the inner product of the damping equation with $\boldsymbol{H}$ yields

$$\frac{\mathrm{d}\theta_i^p}{\mathrm{d}t} = \begin{cases} -\beta \|\boldsymbol{H}\| \sin\theta_i^p, & |\theta_i^p| < \pi/2, \\ -\beta \|\boldsymbol{H}\| (2 - \sin\theta_i^p), & |\theta_i^p| \geq \pi/2, \end{cases} \tag{45}$$

where $\beta$ is a user-defined damping coefficient. Although neglecting the precession term reduces the physical fidelity of the magnetization dynamics, no noticeable artifacts were observed in the reported results [KH22]. Moreover, as mentioned earlier, the magnetization dynamics methods typically exhibit only two regimes (linear growth proportional to $\chi^*$ and saturation), resulting in a non-smooth magnetization curve (Fig. 9a) that is unfavorable for differentiable applications. To overcome this limitation, Kim and Han [KH22] reformulated Eq. (43) as

$$\boldsymbol{H}(\boldsymbol{x}_i) = \boldsymbol{H}^*(\boldsymbol{x}_i) - \frac{1}{f^{-1}(\|\boldsymbol{M}_i\|)} \boldsymbol{M}_i, \tag{46}$$

where $f^{-1}(\|\boldsymbol{M}\|)$ is the inverse of the smooth nonlinear function

$$f(H) = M_\mathrm{s} \tanh\left(\frac{1}{\gamma_\mathrm{D} M_\mathrm{s}} H\right), \tag{47}$$

with the constant $M_\mathrm{s}$ denoting the saturation magnetization magnitude. This formulation preserves the asymptotic behavior of magnetization as $\boldsymbol{H}^* \to 0$ and $\boldsymbol{H}^* \to \infty$, while ensuring a smooth transition between the two regimes. See Fig. 9b.

### 4.2. Medium-Based Approaches

While dipole-based approaches embody the long-standing computer graphics philosophy of discretizing complex phenomena into manageable elements, medium-based approaches reflect the community's deep expertise in developing high-precision numerical solvers. The latter treat the magnetic quantities $\boldsymbol{B}$, $\boldsymbol{H}$, and $\boldsymbol{M}$ as continuous fields and solve in full the partial differential equations (PDEs) defined by Eqs. (30) and (31).

Since medium-based approaches solve the same governing equations under a unified physical model, their physical accuracy and computational complexity are directly comparable. Here, we summarize a qualitative comparison of the solvers to be introduced in this subsection in Tab. 1, while their quantitative comparisons can be found at the end of §4.2.3.

#### 4.2.1. SPH Methods

Inspired by fluid simulation techniques, Huang et al. [HHM19; SHM23] adopted the smoothed particle hydrodynamics (SPH) framework to discretize linearly magnetized continua. Assuming that each particle represents a small uniform volume $V$, the magnetic moment of the $i$-th particle located at $\boldsymbol{x}_i$ is computed as

$$\boldsymbol{m}_i = V\chi \left[\boldsymbol{H}_\mathrm{ext}(\boldsymbol{x}_i) + \boldsymbol{H}_\mathrm{int}(\boldsymbol{x}_i)\right]. \tag{48}$$

Consequently, the magnetization field at any position $\boldsymbol{x}$ in the system can be expressed, following the SPH formulation, as

$$\boldsymbol{M}(\boldsymbol{x}) = \sum_i \boldsymbol{m}_i W(\boldsymbol{x} - \boldsymbol{x}_i, h), \tag{49}$$

where $W(\boldsymbol{r}, h)$ is a smoothing kernel that satisfies

$$\begin{cases} W(\boldsymbol{r}, h) = \dfrac{1}{h^3} w\left(\dfrac{\|\boldsymbol{r}\|}{h}\right), & \text{(50a)} \\ \iiint_{\mathbb{R}^3} W(\boldsymbol{r}, h)\, \mathrm{d}V = 1, & \text{(50b)} \end{cases}$$

with $w(r)$ being a Gaussian-like kernel function.

According to the superposition principle, substituting Eq. (49) into the governing equation (30) yields

$$\boldsymbol{H}_\mathrm{int}(\boldsymbol{x}) = -\nabla\phi(\boldsymbol{x}) = -\sum_i \nabla\phi_i(\boldsymbol{x}), \tag{51}$$

where $\phi_i(\boldsymbol{x})$ satisfies the following Poisson equation:

$$\begin{cases} \nabla^2\phi_i(\boldsymbol{x}) = \nabla \cdot \boldsymbol{m}_i\, W(\boldsymbol{x} - \boldsymbol{x}_i, h), & \text{(52a)} \\ \phi_i(\boldsymbol{x}) \to 0 \quad \text{as} \quad \|\boldsymbol{x}\| \to \infty. & \text{(52b)} \end{cases}$$

Using the gradient, divergence, and Laplacian operators defined in SPH formulations, Huang et al. [HHM19] solved the system (52) and derived an analytical expression for the magnetic field contribution of each particle:

$$-\nabla\phi_i(\boldsymbol{x}) = \boldsymbol{\eta}(\boldsymbol{x} - \boldsymbol{x}_i, \boldsymbol{m}_i), \tag{53}$$

$$\boldsymbol{\eta}(\boldsymbol{r}, \boldsymbol{m}) = \left[W_\mathrm{avg}(\boldsymbol{r}) - W(\boldsymbol{r})\right] \hat{\boldsymbol{r}}(\boldsymbol{m} \cdot \hat{\boldsymbol{r}}) - \frac{W_\mathrm{avg}(\boldsymbol{r})}{3} \hat{\boldsymbol{m}}, \tag{54}$$

where $W_\mathrm{avg}(\boldsymbol{r})$ denotes the average kernel value within a sphere of radius $\|\boldsymbol{r}\|$:

$$W_\mathrm{avg}(\boldsymbol{r}) = \frac{3}{\|\boldsymbol{r}\|^3} \int_0^{\|\boldsymbol{r}\|} W(\xi)\, \xi^2\, \mathrm{d}\xi. \tag{55}$$

Note that the smoothing radius $h$ is a fixed constant and is thus omitted from the kernel arguments for brevity.

Substituting Eq. (48) into Eq. (51) and adding the result to Eq. (49), by evaluating at each SPH particle center, we obtain

$$\frac{\boldsymbol{B}(\boldsymbol{x}_i)}{\mu_0} - \boldsymbol{H}_\mathrm{ext}(\boldsymbol{x}_i) = \sum_j \left[\boldsymbol{\eta}(\boldsymbol{x}_i - \boldsymbol{x}_j, \boldsymbol{m}_j) + \boldsymbol{m}_j\, W(\boldsymbol{x}_i - \boldsymbol{x}_j)\right]. \tag{56}$$

It is straightforward to see that the right-hand side is a linear combination of the unknown moments $\{\boldsymbol{m}_i\}$. With $\boldsymbol{m}_i \approx V\chi \boldsymbol{B}(\boldsymbol{x}_i)/(1+\chi)\mu_0$, the above equation can be rewritten as a linear system with respect to $\{\boldsymbol{B}(\boldsymbol{x}_i)\}$. This system is symmetric, but its positive definiteness is not guaranteed. Therefore, Huang et al. [HHM19] proposed solving it in the least-squares sense using the *conjugate gradient for least squares (CGLS)* method. Moreover, since $\boldsymbol{\eta}(\boldsymbol{r}, \boldsymbol{m})$ is non-compactly supported, the resulting linear system is dense, and the matrix–vector product evaluation becomes computationally expensive. However, noting that Eq. (54) asymptotically reduces to Eq. (8) when $\|\boldsymbol{r}\| \gg h$, the summation can be accelerated via the *fast multipole method (FMM)* [BG97]. This optimization reduces the computational cost of a single system evaluation from $O(N^2)$ to $O(N)$, where $N$ denotes the number of SPH particles.

**Smoothed susceptibility.** The interpolation based on SPH particles smooths physical quantities such as the susceptibility $\chi$. This eliminates the discontinuity on the right-hand side of Eq. (30). As observed by Huang et al. [HHM19], the transition layer of $\chi$ is approximately $2h$ thick. See Fig. 10 for illustration.

**Table 1:** *Comparisons among medium-based magnetostatic solvers. In each column, the cells with properties that are preferred due to correctness or simplicity are colored light green. Here, $K$ denotes the number of iterations, and $N$ denotes the number of boundary vertices that are input into BEM solvers. For SPH solvers, $N\sqrt{N} \approx N_\mathrm{p}$, where $N_\mathrm{p}$ denotes the number of SPH particles; for FDM solvers, $N\sqrt{N} \approx n^3$, where $n$ is the grid resolution. Source: Ni et al. [NWWC24].*

| Approach | Physical accuracy | | Linear system | | Computational complexity | |
|---|---|---|---|---|---|---|
| | Sharp interface | BC at infinity | Sparsity | Method | Time | Space |
| SPH [HHM19; SHM23] | No | Yes | Dense | CGLS | $O(KN\sqrt{N})$ | $O(N\sqrt{N})$ |
| FDM [NZWC20; SNZ*21] | No | No | Sparse | GMGPCG | $O(KN\sqrt{N})$ | $O(N\sqrt{N})$ |
| BEM [HM20] | Yes | Yes | Dense | PGMRES | $O(KN^2)$ | $O(N^2)$ |
| BEM [NWWC24] | Yes | Yes | Dense | FPI | $O(KN)$ | $O(N)$ |

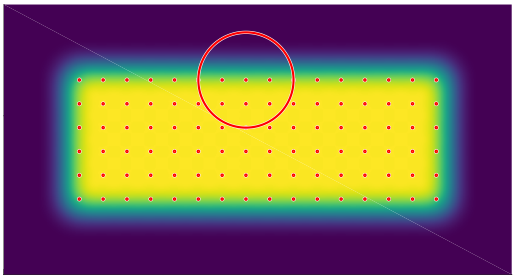

**Figure 10:** *The SPH method smooths the susceptibility $\chi$, which is constant within the center region of the continuum (colored yellow) and drops quickly down to zero beyond the boundary (colored dark blue). A transition layer of approximately $2h$ is observed. The SPH particles are plotted as red dots, while the red circle indicates the support of the kernel function. The distance between adjacent particles is given by $h$. Source: Huang et al. [HHM19].*

#### 4.2.2. Finite Difference Methods

Unlike the SPH method, which discretizes physical fields using randomly distributed particles, finite difference methods (FDMs) are built upon regular background grids. In this framework, physical quantities are stored at grid nodes, while values between nodes are interpolated using trilinear interpolation. The distance between adjacent nodes is referred to as the grid spacing, denoted by $\Delta x$.

Ni et al. [NZWC20] observed that under the assumption of linear magnetization, Eq. (30) can be reformulated as $\nabla^2\phi = \nabla\cdot\chi(\boldsymbol{H}_\mathrm{ext} - \nabla\phi)$, which leads to

$$\nabla\cdot(1+\chi)\nabla\phi = \nabla\cdot\chi\boldsymbol{H}_\mathrm{ext}, \tag{57}$$

a Poisson equation with spatially varying coefficients. Here, $\chi$ is no longer a material-specific constant but rather a spatial field that takes different values in different media. In an ideal setting, $\chi$ exhibits discontinuities across material interfaces, which makes Eq. (57) challenging to solve in its discrete form. To address this issue, Ni et al. [NZWC20] employed a smoothed Heaviside step function $\tilde{\theta}$ to regularize the interface between two media with magnetic susceptibilities $\chi_1$ and $\chi_2$:

$$\chi(\boldsymbol{x}) = [1-\tilde{\theta}(\varphi(\boldsymbol{x}))]\,\chi_1 + \tilde{\theta}(\varphi(\boldsymbol{x}))\,\chi_2, \tag{58}$$

$$\tilde{\theta}(\varphi) = \begin{cases} 0, & \varphi \le -\varepsilon, \\ \frac{1}{2} + \frac{\varphi}{2\varepsilon} + \frac{1}{2\pi}\sin\frac{\pi\varphi}{\varepsilon}, & |\varphi| < \varepsilon, \\ 1, & \varphi \ge +\varepsilon \end{cases} \tag{59}$$

where $\varphi(\boldsymbol{x})$ denotes the signed distance function (SDF) of the 1st medium (positive outside and negative inside), and $\varepsilon$ is the interface thickness parameter, typically chosen as a small multiple of $\Delta x$. In Appendix A, we analyze, in a simplified setting, how such a diffuse-interface regularization of $\chi$ modifies the interfacial magnetic force balance and quantify the leading-order error induced by smoothing a physically sharp magnetic interface.

Discretizing Eq. (57) using FDM is straightforward. To improve numerical accuracy, Ni et al. [NZWC20] adopted a marker-and-cell (MAC) grid [HW65], where $\phi$ and $\chi$ are stored at cell centers, while $\boldsymbol{H}_\mathrm{ext}$ is stored at cell faces. Taking the 1D case as an example, the finite difference scheme with spatially varying coefficients for cell $i$ can be written as

$$\begin{aligned} &\frac{(1+\chi_{i+1/2})(\phi_{i+1}-\phi_i) - (1+\chi_{i-1/2})(\phi_i-\phi_{i-1})}{(\Delta x)^2} \\ &\quad = \frac{\chi_{i+1/2}(h_{i+1}-h_i) - \chi_{i-1/2}(h_i-h_{i-1})}{\Delta x}, \end{aligned} \tag{60}$$

where $h$ denotes the 1D component of $\boldsymbol{H}_\mathrm{ext}$. The integer subscripts $i$, $i-1$, and $i+1$ represent cell indices, while the half indices refer to cell faces. Applying this construction to all $i$ yields a symmetric, positive-definite, and sparse linear system, which can naturally be solved efficiently using a *geometric multigrid-preconditioned conjugate gradient (GMGPCG)* solver [MST10].

It should be noted, however, that FDMs suffer from a significant limitation: the computational domain covered by the grid is finite, making it difficult to naturally impose the far-field boundary condition (31). In practice, one often has to enlarge the grid as much as possible and approximate Eq. (31) by enforcing the Neumann boundary condition $\partial\phi/\partial n = 0$ on the grid boundary. For magnetic modeling, this is equivalent to enclosing the system in a metallic box, preventing magnetic field lines from leaving the domain—effectively introducing a form of *magnetic shielding*. The quantitative error introduced by this finite-domain Neumann truncation, and its scaling with the size of the computational domain, are analyzed analytically in Appendix B. In addition, it is possible—and worthy of further investigation—to impose far-field conditions

more accurately within FDMs by using methods such as artificial boundary conditions [Hou13] or Kelvin transformations [NRC21].

**Nonlinear magnetization.** FDMs can also be employed to determine magnetic fields in materials with nonlinear magnetization. Sun et al. [SNZ*21] discretized Eq. (30) on a collocated grid, where all physical quantities are stored at the same cell location, using finite-difference approximations of the nabla operator [RSG*08]. In their formulation, the magnetization $\boldsymbol{M}(\boldsymbol{H})$ follows the nonlinear magnetization curve described by Eq. (12). Let $\tilde{\boldsymbol{\phi}} = (\phi_1, \phi_2, \ldots, \phi_N)$ denote the vector of scalar potentials at all grid points, where $N$ is the total number of nodes. Sun et al. [SNZ*21] observed that, owing to the monotonicity of the Langevin function, the Jacobian matrix $\partial \boldsymbol{F}/\partial \tilde{\boldsymbol{\phi}} \in \mathbb{R}^{N\times N}$ of the discretized nonlinear system $\boldsymbol{F}(\tilde{\boldsymbol{\phi}}) = \boldsymbol{0}$ is always symmetric and semi-positive definite. This property allows the system to be efficiently solved via the Newton–Raphson method, achieving quadratic convergence toward the solution.

### 4.2.3. Boundary Element Methods

Under the assumption of linear magnetization, the magnetization can always be obtained from the magnetic induction as $\boldsymbol{M} = \chi \boldsymbol{B}/(1+\chi)$. This implies that the divergence of $\boldsymbol{M}$ vanishes inside the medium, causing the right-hand side of Eq. (30) to vanish as well. Across material interfaces, however, $\boldsymbol{M}$ exhibits discontinuities. By applying the divergence theorem to a small pillbox volume straddling the boundary, we can derive

$$\nabla^2 \phi = (\boldsymbol{M}_2 - \boldsymbol{M}_1) \cdot \boldsymbol{n}\, \delta_\Gamma, \tag{61}$$

where $\boldsymbol{n}$ is the unit normal pointing from medium 1 to medium 2, $\delta_\Gamma$ is the generalized Dirac delta function on the boundary $\Gamma$, and the subscripts indicate limits taken on each side of the boundary.

Considering that the solution to

$$\begin{cases} \nabla^2 G(\boldsymbol{x},\boldsymbol{x}') = -\delta(\|\boldsymbol{x}-\boldsymbol{x}'\|), & \forall \boldsymbol{x}, \quad (62a) \\ G(\boldsymbol{x},\boldsymbol{x}') \to 0, & \|\boldsymbol{x}\| \to \infty \quad (62b) \end{cases}$$

is $G(\boldsymbol{x},\boldsymbol{x}') = 1/(4\pi\|\boldsymbol{x}-\boldsymbol{x}'\|)$, it is natural to define

$$\sigma(\boldsymbol{x}) = -(\boldsymbol{M}_2 - \boldsymbol{M}_1)\cdot \boldsymbol{n}, \qquad \boldsymbol{x} \in \Gamma, \tag{63}$$

such that the solution to Eq. (61) can be formulated as

$$\phi(\boldsymbol{x}) = \iint_\Gamma G(\boldsymbol{x},\boldsymbol{x}')\,\sigma(\boldsymbol{x}')\,\mathrm{d}\Gamma', \qquad \forall \boldsymbol{x}, \tag{64}$$

which is termed the *single-layer potential*. By taking the normal derivative of Eq. (64), we can further obtain

$$\left[\frac{\partial \phi}{\partial n}(\boldsymbol{x})\right]_\pm = \iint_\Gamma \frac{\partial G}{\partial n}(\boldsymbol{x},\boldsymbol{x}')\,\sigma(\boldsymbol{x}')\,\mathrm{d}\Gamma' \mp \frac{1}{2}\sigma(\boldsymbol{x}), \quad \boldsymbol{x} \in \Sigma, \tag{65}$$

where the superscripts "+" and "−" correspond to the limits taken from media 2 and media 1, respectively. Substituting Eq. (65) into Eq. (63), it is straightforward to show that

$$\frac{\sigma(\boldsymbol{x})}{2\alpha} = -\iint_\Gamma \frac{\partial G}{\partial n}(\boldsymbol{x},\boldsymbol{x}')\,\sigma(\boldsymbol{x}')\,\mathrm{d}\Gamma' + \boldsymbol{H}_{\text{ext}}(\boldsymbol{x})\cdot\boldsymbol{n}, \quad \boldsymbol{x}\in\Gamma, \tag{66}$$

where $\alpha = (\chi_1 - \chi_2)/(2+\chi_1+\chi_2)$ is the reduced permeability.

In Eq. (66), the only unknown is the surface function $\sigma(\boldsymbol{x})$. Ni et al. [NWWC24] proposed to discretize the boundary $\Gamma$ into a point cloud $\{\boldsymbol{x}_i\}$, each associated with a scalar value $\sigma_i$, surface area element $\Delta A_i$, and normal vector $\boldsymbol{n}_i$. The unknowns can then be solved through a fixed-point iteration (FPI) of the form

$$\sigma_i = -2\alpha \sum_j \frac{\partial G}{\partial n_i}(\boldsymbol{x}_i,\boldsymbol{x}_j)\,\sigma(\boldsymbol{x}_j)\,\Delta A_j + 2\alpha \boldsymbol{H}_{\text{ext}}(\boldsymbol{x}_i)\cdot\boldsymbol{n}_i. \tag{67}$$

They further showed that when $|\alpha| < 1$, the FPI scheme is guaranteed to converge as long as the point cloud is sufficiently dense. Since the kernel $\partial G/\partial n_i = \nabla G \cdot \boldsymbol{n}_i$ involves a fixed normal $\boldsymbol{n}_i$ during summation, the computation can be efficiently accelerated using the fast multipole method (FMM), reducing the per-iteration complexity from $O(N^2)$ to $O(N)$, where $N$ denotes the number of surface samples. It is worth noting that Eqs. (64), (65), and (66) are all boundary integral equations (BIEs). Solving a volumetric problem by reformulating it as a BIE lays the foundation of the boundary element method (BEM) [SS11].

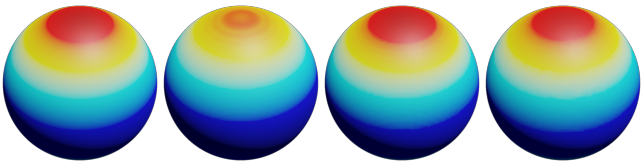

**(a)** *Ground truth;* **(b)** *FDM'20* ($\epsilon \approx 8.39\%$); **(c)** *BEM'20* ($\epsilon \approx 1.80\%$); **(d)** *BEM'24* ($\epsilon \approx 2.44\%$).

**Figure 11:** *Comparison of different solvers with respect to accuracy of the magnetic pressure on a sphere surface. Higher pressure is mapped to warmer color in the visualization, and the maximum relative error of each solver is reported in the captions. Source: Ni et al. [NWWC24].*

**Double-layer potential.** In contrast to Ni et al. [NWWC24], who derived and solved the single-layer potential formulation, Huang and Michels [HM20] developed a BEM approach based on the double-layer potential. Suppose the magnetic scalar potential of the external field, $\phi_{\text{ext}}$, is known (with $\boldsymbol{H}_{\text{ext}} = -\nabla\phi_{\text{ext}}$). Starting from the single-layer potential $\phi$, we can define a modified potential

$$\phi^* = \mu\phi + (\mu - \mu_0)\phi_{\text{ext}}, \tag{68}$$

which satisfies $\boldsymbol{B}_{\text{int}} = -\nabla\phi^*$. Analogous to the single-layer case, a surface density $\sigma^*$ can be introduced such that the following boundary integral equations hold:

$$\phi^*(\boldsymbol{x}) = \iint_\Gamma \frac{\partial G}{\partial n'}(\boldsymbol{x},\boldsymbol{x}')\,\sigma^*(\boldsymbol{x}')\,\mathrm{d}\Gamma', \qquad \boldsymbol{x}\notin\Gamma, \tag{69}$$

$$\frac{\sigma^*(\boldsymbol{x})}{2\alpha} = -\iint_\Gamma \frac{\partial G}{\partial n'}(\boldsymbol{x},\boldsymbol{x}')\,\sigma^*(\boldsymbol{x}')\,\mathrm{d}\Gamma' - \mu_0\phi_{\text{ext}}. \tag{70}$$

Unlike Ni et al. [NWWC24], who employed a lightweight Nyström method [TC20], Huang and Michels [HM20] used a Galerkin formulation on a linearly interpolated triangular mesh to explicitly assemble the linear system, which was then solved using a *preconditioned generalized minimal residual (PGMRES)* solver [SS86]. Because the normal vector $\boldsymbol{n}'$ in the kernel $\partial G/\partial n'$ varies across the surface, FMM cannot be applied for acceleration. Consequently, both the evaluation cost per iteration and the memory footprint of

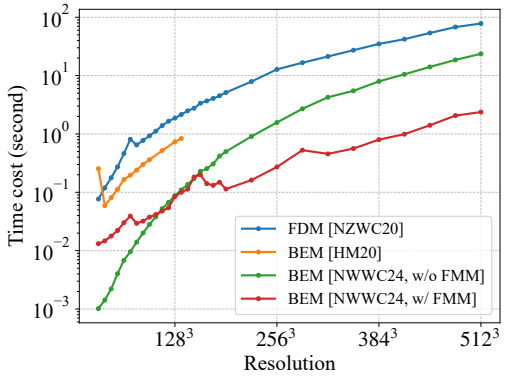


**Figure 12:** *Comparison of different solvers in terms of computation time on Eulerian grids with various resolutions. The timing measurement starts when a solver achieves a relative residual reduction below $10^{-6}$. Note that only the BEM solver of Huang and Michels [HM20] is implemented with GPU acceleration and is limited to handling resolutions no greater than $136^3$ due to memory constraints arising from the assembly of dense matrices. For the BEM solver of Ni et al. [NWWC24], there is a large constant factor in the time complexity of the FMM-accelerated verison. A direct summation version can be a better choice with resolutions lower than $100^3$. Source: Ni et al. [NWWC24].*

the system scale as $O(N^2)$, where $N$ denotes the number of mesh vertices.

**Accuracy and efficiency.** To quantitatively compare the accuracy and efficiency of three representative magnetostatic solvers: the FDM of Ni et al. [NZWC20], the BEM of Huang and Michels [HM20], and the BEM of Ni et al. [NWWC24], a benchmark scenario is constructed. a magnetic sphere ($r = 1\,\mathrm{m}$, $\chi = 1$) is centered at the origin. Under an external magnetic field $\boldsymbol{H}_{\mathrm{ext}} = (0, 1\,\mathrm{A\,m^{-1}}, 0)$, the total magnetic field inside the sphere becomes $\boldsymbol{H} = (0, 0.75\,\mathrm{A\,m^{-1}}, 0)$, yielding an analytical solution for the interfacial magnetic pressure (see Eq. (74)). On a Cartesian grid of resolution $128^3$, covering the domain $-2\,\mathrm{m} \le x, y, z \le 2\,\mathrm{m}$, all methods are evaluated. The input mesh for the BEMs is extracted from this grid using marching cubes [LC87], and the results are shown in Fig. 11. Across grid resolutions ranging from $32^3$ to $512^3$, the time required for each solver to reduce the relative residual below $10^{-6}$ is plotted in Fig. 12. In terms of accuracy, the Galerkin-based BEM of Huang and Michels [HM20] achieves the highest precision. In contrast, the fixed-point BEM of Ni et al. [NWWC24] demonstrates the lowest spatial and temporal complexity, offering superior computational efficiency.

## 5. Magnetic Material Simulations

Having established the theoretical foundations (§2–3) and magnetostatic solvers (§4), what remains is the evaluation of magnetic forces and their integration into traditional physical simulation pipelines. In general, the choice of simulation methods, frameworks, and pipelines is closely tied to the nature of the underlying materials. Accordingly, we categorize and summarize existing simulation frameworks that can be extended to incorporate magnetic effects, based on three representative material types: rigid bodies, elastic bodies, and fluids.

**Figure 13:** *Snapshots of an interactive simulation in which soft ferromagnetic spheres are lifted by a permanent magnet. Source: Thomaszewski et al. [TGPS08].*

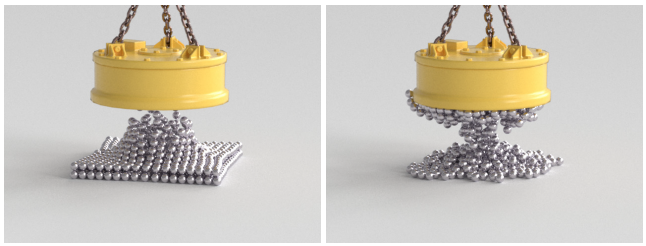

**Figure 14:** *The crane magnet and a large number of soft ferromagnets. Source: Kim et al. [KPH18].*

### 5.1. Magnetic Rigid Bodies

Magnetic rigid bodies, or simply magnets, are the most common form of magnetic matter encountered in everyday life, and their behaviors are the most familiar to us. Since a rigid body possesses only six (three translational and three rotational) degrees of freedom (DoFs), its dynamical simulation is relatively straightforward. With collisions, contacts, and friction unaltered, the rigid-body simulation pipelines do not differ substantially. Therefore, the key challenge in incorporating magnetic effects lies primarily in modeling and computing the magnetic forces themselves.

#### 5.1.1. Equivalent Dipole Methods

As discussed earlier, a common approach in magnetic rigid-body simulation is to discretize each rigid body into a collection of small cells, each carrying an embedded dipole $\boldsymbol{m}_i$. This representation not only facilitates the computation of magnetization but also enables the evaluation of magnetic forces within the same framework. Kim and Han [KH20] referred to such a force model as *equivalent dipole methods (EDMs)*.

As introduced in §2.4, the force exerted on a magnetic dipole in a field is given by Eq. (18). Naturally, the total magnetic force acting on a rigid body can be obtained by summing the contributions of all constituent dipoles:

$$\boldsymbol{F}_{\mathrm{m}} = \sum_i \nabla[\boldsymbol{m}_i \cdot \boldsymbol{B}(\boldsymbol{x}_i)]. \tag{71}$$

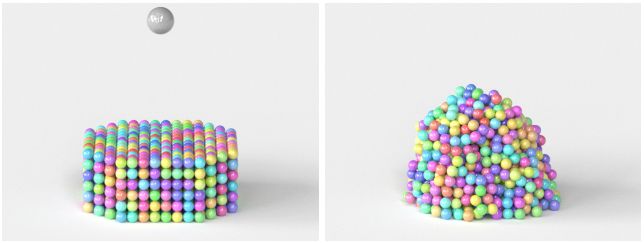

**Figure 15:** *A heavy and strong sphere magnet falls down and strikes the metal balls. Source: Kim and Han [KH22].*

**Figure 16:** *A magnetizable ball is running indefinitely from the funnel into the tracks and loops back into the funnel. The additional momentum for the ball to loop back into the funnel is provided by turning on and off an electromagnet at the correct time. Source: Westhofen et al. [WFJB24].*

These forces induce a moment about the body's reference point (typically the center of mass), known as the *mechanical torque*:

$$\boldsymbol{\tau}_{\mathrm{m}} = \sum_i (\boldsymbol{x}_i - \boldsymbol{x}_{\mathrm{c}}) \times \nabla [\boldsymbol{m}_i \cdot \boldsymbol{B}(\boldsymbol{x}_i)]. \tag{72}$$

However, this mechanical torque does not account for all torque components. When a dipole moment $\boldsymbol{m}_i$ is misaligned with the local magnetic field $\boldsymbol{B}$, the external field exerts an aligning torque on it, as defined in Eq. (17). Since this internal pair of torques cancels out in terms of net force, it produces the same resultant torque with respect to any reference point. By summing the contributions of all dipoles, we obtain the magnetic torque:

$$\boldsymbol{\tau}^*_{\mathrm{m}} = \sum_i \boldsymbol{m}_i \times \boldsymbol{B}(\boldsymbol{x}_i). \tag{73}$$

In systems without hard-magnetic materials, this magnetic torque term can typically be neglected.

Substituting Eqs. (71–73) into the rigid-body governing equations (32) and integrating them using an explicit Euler scheme yields a straightforward simulation pipeline for magnetic rigid bodies [TGPS08; KPH18; KH22]. Standard treatments for contact and friction can be adopted from Andrews et al.'s SIGGRAPH course [AEF22]. In addition, Kim and Han [KH22] observed that treating $\boldsymbol{m}_i$ as a variable rather than a constant when evaluating the gradient in Eq. (71) can significantly improve numerical stability, though the two formulations are theoretically equivalent—differing only in how the force components are categorized (see §2.4).

We refer the reader to Figs. 13–15 for simulation results of EDM pipelines, which mainly differ in their magnetostatic solvers.

**Strongly coupled simulation.** The aforementioned framework is weakly coupled, since the computation of forces (including magnetic, contact, and frictional forces) is performed asynchronously with respect to the rigid bodies' state updates at each time step. To address this limitation, Westhofen et al. [WFJB24] introduced an optimization-based, strongly coupled formulation by combining the incremental potential contact (IPC) energy [FLS*21] with the dipole magnetic potential energy, $W_{\mathrm{m}} = -\sum_i \boldsymbol{m}_i \cdot \boldsymbol{B}(\boldsymbol{x}_i)$. In each time step, the dipoles of non-permanent magnets are first determined following the procedure in §4.1.1. These magnetic moments are then fixed and rigidly attached to the bodies as those belonging to permanent magnets, after which all dipoles are jointly handled within a unified optimization problem solved using Newton's method. This scheme is therefore semi-implicit in nature. To further improve numerical conditioning, Westhofen et al. [WFJB24] proposed considering only near-field dipole–dipole interactions within the optimization, while treating long-range interactions explicitly to reduce the condition number of the Hessian matrix. See Fig. 16 for a simulation experiment using this scheme.

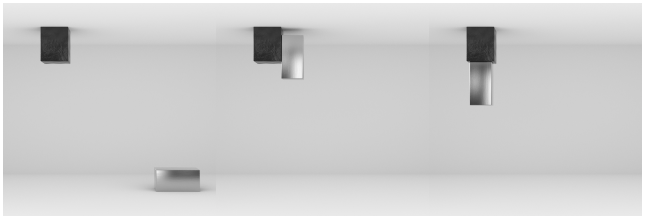

**(a)** *Initial frame;* **(b)** *Simulation w/o* $\boldsymbol{H}_{\mathrm{int}}$*;* **(c)** *Simulation w/* $\boldsymbol{H}_{\mathrm{int}}$*;*

**Figure 17:** *An iron box is attracted by a permanent magnet. The simulation result is visually realistic only if the internal field has been correctly solved. Source: Ni et al. [NZWC20].*

**Figure 18:** *A cubic magnet stably attracts 243 small metal balls, simulated by integrating the BEM-based magnetostatic solver into Bullet Physics SDK [Cou15]. Source: Ni et al. [NWWC24].*

### 5.1.2. Magnetic Boundary Methods

A rigid body can be regarded as a magnetic medium, and the magnetic force within such a medium can take multiple forms (see §2.4). Examining the Helmholtz force in Eq. (26), Ni et al. [NZWC20; NWWC24] observed that it is proportional to $\nabla\chi$, and thus vanishes inside linearly magnetized materials with spatially uniform susceptibility. In this case, the net magnetic action on the object reduces to the pressure difference caused by the discontinuity of the magnetic stress $\boldsymbol{T} \cdot \boldsymbol{n}$ across the boundary. Kim and Han [KH20] referred to this class of models as magnetic boundary methods (MBMs).

Assuming a susceptibility $\chi$ for the magnetic material and $\chi =$

**Figure 19:** *The huge crane magnet pulls up the metal junks. The thin, sharp and complex materials are stably simulated. Source: Kim and Han [KH20].*

0 in air, and adopting the Minkowski formulation, the magnetic pressure acting on the boundary can be expressed as

$$p_{\mathrm{m}} = \frac{1}{2}\mu_0\chi\|\boldsymbol{H}\|^2 + \frac{1}{2}\mu_0(\chi\boldsymbol{H}\cdot\boldsymbol{n})^2, \tag{74}$$

where $\boldsymbol{H}$ is evaluated on the material side of the interface. This pressure always acts inward, perpendicular to the object's surface.

In computer graphics, rigid bodies are typically represented by surface meshes. By evaluating Eq. (74) at each vertex $\boldsymbol{x}_i$ of the mesh, the total magnetic force and torque on the rigid body can be computed as

$$\boldsymbol{F}_{\mathrm{m}} = -\sum_i [p(\boldsymbol{x}_i)\,\Delta A_i]\,\boldsymbol{n}_i, \tag{75}$$

$$\boldsymbol{\tau}_{\mathrm{m}} = -\sum_i [p(\boldsymbol{x}_i)\,\Delta A_i]\,(\boldsymbol{x}_i - \boldsymbol{x}_c)\times\boldsymbol{n}_i, \tag{76}$$

where $\boldsymbol{n}_i$ denotes the outward-pointing normal and $\Delta A_i$ denotes the control area, associated with the $i$-th vertex. Substituting these expressions into an existing rigid-body dynamics framework directly enables the simulation of magnetic rigid bodies.

To evaluate the magnetic field required in Eq. (74), Ni et al. [NZWC20; NWWC24] proposed two complementary solutions based on FDM and BEM. In the FDM approach, the rigid body is first embedded in a background grid, from which its SDF $\varphi$ is constructed. A linear system is then solved following the procedure described in §4.2.2, and the boundary field value $\tilde{\boldsymbol{H}}$ is obtained via interpolation. Since FDM inherently smooths the boundary, the resulting $\boldsymbol{H}$-field near the interface is also smoothed. An equivalent form of the magnetic pressure, accounting for this smoothing effect, is given as [NZWC20]:

$$p_{\mathrm{m}} = \frac{1}{2}\mu_0\chi\|\tilde{\boldsymbol{H}}\|^2 + \frac{1}{8(\chi+1)}\mu_0(\chi\tilde{\boldsymbol{H}}\cdot\boldsymbol{n})^2. \tag{77}$$

Unlike FDM, BEM directly solves for the magnetic field on the boundary without discretizing the surrounding volume, making it particularly well-suited for MBMs. Combining BEM with MBM is thus straightforward and requires no additional effort [NWWC24]. We demonstrate the results of MBMs coupling with FDM and BEM in Figs. 17 and 18, respectively.

Alternatively, Kim and Han [KH20] derived MBMs from the magnetic vector potential formulation [Jac98]:

$$\boldsymbol{A}(\boldsymbol{x}) = \frac{\mu_0}{4\pi}\iiint_V \boldsymbol{M}(\boldsymbol{x}')\times\frac{\boldsymbol{x}-\boldsymbol{x}'}{\|\boldsymbol{x}-\boldsymbol{x}'\|^3}\,\mathrm{d}V'. \tag{78}$$

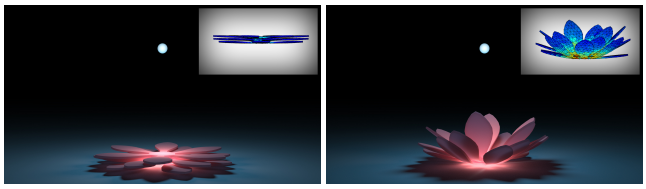

**Figure 20:** *A soft magnetic lotus attracted by a moving magnet, with deformations demonstrated by the von Mises strain distribution in the upper-right corner. Source: Ni et al. [NZWC20].*

When the magnetization $\boldsymbol{M}$ inside the object is uniform, $\boldsymbol{M}$ can be taken outside the integral, and the remaining volume integral can be converted into a surface integral using the divergence theorem. Similarly, the magnetic induction $\boldsymbol{B} = \nabla\times\boldsymbol{A}$ can be evaluated via surface integration, allowing $\boldsymbol{F}_{\mathrm{m}}$, $\boldsymbol{\tau}_{\mathrm{m}}$, and $\boldsymbol{\tau}^*_{\mathrm{m}}$ to be expressed purely in boundary-integral form. Unlike the pressure-based formulation above, this approach assumes each rigid body has a homogeneous magnetization. To accommodate arbitrarily shaped bodies, Kim and Han [KH20] approximated each rigid body as one cell with two submagnetizations. See Fig. 19 for an experiment.

**EDM vs. MBM.** Similar to our conclusions in the discussion of magnetic force formulations (§2.4), when the system contains only linearly magnetized materials, the latter (MBM) can achieve more accurate results with lower computational complexity, even if complex geometries or strong mutual induction are present. However, in terms of ease of implementation, numerical stability, and generalizability, EDM often exhibits distinct advantages.

### 5.2. Magnetic Elastic Bodies

Magnetic elastic bodies have significant applications in areas such as magnetic soft robotics. With the advancement of technologies like 3D printing, researchers can now freely design elastic bodies whose magnetization varies spatially, and control their motion through externally applied magnetic fields [ZKC*19; WKGZ20; YPC*21]. Compared with rigid bodies, the dynamics of elastic bodies are more complex. In computer graphics, two commonly used frameworks for elastic body simulation are based on the finite element method (FEM) [SB12] and the material point method (MPM) [JST*16]. The former excels at modeling elastic solids, whereas the latter can also be extended to simulate viscoelastic fluids, such as magnetic clay.

#### 5.2.1. FEM Frameworks

For weakly coupled simulations, incorporating magnetic forces into a FEM framework is relatively straightforward. We can simply compute the magnetic body force density at the vertices of tetrahedral or hexahedral elements, or equivalently, the magnetic pressure at the vertices of surface elements (triangles or quads), and directly apply these forces within an existing FEM solver. Ni et al. [NZWC20] adopted this approach by combining the magnetic field computed via FDM with the magnetic pressure formulation of MBM (Eq. (77)), integrating both into an FEM-based elastic solver. The implementation closely parallels the rigid-body case, with the

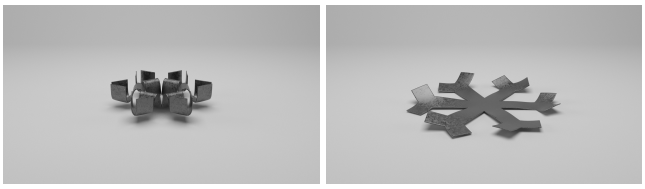

**Figure 21:** *A deforming thin-shell hexagram, which is consistent with real-world experiments [KPLZ19]. Left: curling up; right: arm-shaking. The magnetization profile is optimized using the implicit FEM framework. Source: Chen et al. [CNZ*22].*

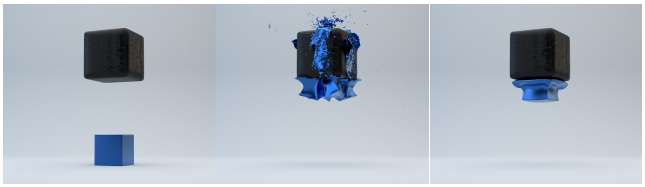

**(a)** *Initial frame;* **(b)** *Linear solver;* **(c)** *Nonlinear solver.*

**Figure 22:** *A square magnetic elastic solid is attracted toward a permanent magnet. Under the same MPM framework, the simulation crashes when a magnetostatic solver restricted to linear magnetization is used. Source: Sun et al. [SNZ*21].*

primary additional cost being the computation of the elastic body's SDF $\varphi$ on the background grid. Leveraging this framework, the simulation results are shown in Fig. 20.

For strongly coupled cases, where magnetic and mechanical effects must be solved simultaneously, the formulation simplifies considerably when only hard-magnetic materials are present. In this scenario, it suffices to include the magnetic energy density $w = -\boldsymbol{M} \cdot \boldsymbol{B}$ in the total potential energy of the system. Building upon this idea, Chen et al. [CNZ*22] further neglected the influence of the induced internal field and approximated the magnetic energy density as

$$w \approx -\boldsymbol{M} \cdot \boldsymbol{B}_{\text{ext}} = -J^{-1} \left( \boldsymbol{F} \overline{\boldsymbol{M}} \right) \cdot \boldsymbol{B}_{\text{ext}}. \tag{79}$$

This magnetic term, along with its Jacobian and Hessian with respect to vertex positions, is incorporated into an implicit Euler integration scheme alongside the StVK thin-shell elastic model. Notably, this framework is fully differentiable: using the adjoint method, we can efficiently compute derivatives of the simulated motion of magnetic thin shells with respect to either the rest-state magnetization $\overline{\boldsymbol{M}}$ or the external magnetic field $\boldsymbol{B}_{\text{ext}}$. By defining an objective function and performing gradient-based optimization, Chen et al. [CNZ*22] demonstrated the design and motion control of magnetically actuated thin-shell robots. See Fig. 21 for the example that virtualizes a real-world ferromagnetic soft robot.

### 5.2.2. MPM Frameworks

MPM provides a unified framework for simulating deformable continua. As a hybrid approach combining particles and grids, MPM leverages the advantages of the former in material tracking and the latter in field computation. Sun et al. [SNZ*21] proposed to transfer the magnetization $\boldsymbol{M}$ stored on grid nodes to magnetic moments $\boldsymbol{m}$ on particles during the grid-to-particle (G2P) step. These moments are then advected with the particles to their new positions and subsequently mapped back to the grid during the particle-to-grid (P2G) step, forming the initial $\boldsymbol{M}$-field for the next time step. This field serves as an initial guess for the finite difference magnetostatic solver designed for nonlinearly magnetized materials (see §4.2.2), thereby accelerating the convergence of Newton iterations.

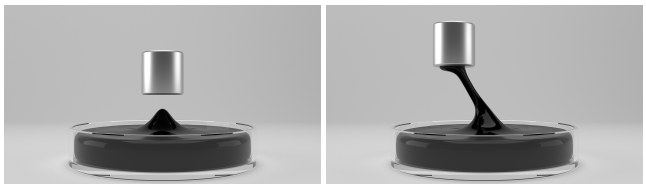

**Figure 23:** *A lump of magnetic clay (viscoelastic fluid) in a container is attracted by a magnet, generating a spike. Source: Sun et al. [SNZ*21].*

In conventional FDM-based field solvers, spatially varying magnetic susceptibility often requires smoothing through SDFs and smoothed step functions, which can be computationally expensive. The particle representation in MPM naturally eliminates this overhead. Assuming Langevin paramagnetism (12), the magnetization $\boldsymbol{M}$ is proportional to the particle number density $n$, which can be computed at grid nodes through the P2G process by weighted accumulation of the microscopic particle counts represented by MPM particles. This grid-based $n$-field is inherently smooth, leading to a correspondingly smooth right-hand side in the governing equation (30). As a result, the magnetostatic field can be solved more robustly without explicit spatial filtering.

When nonlinear magnetization is considered, the volumetric magnetic body force within the material can no longer be neglected. Meanwhile, due to the smoothed boundary treatment, there is no jump in the Maxwell stress tensor, and thus no magnetic pressure arises. Under these conditions, Sun et al. [SNZ*21] adopted the Kelvin force (22) as their magnetic force model, successfully simulating magnetized elastic solids and viscoelastic fluids. Notably, the inclusion of nonlinear magnetization not only enhances physical fidelity but also naturally limits the magnitude of the magnetic force, which substantially improves numerical stability (Fig. 22).

Historically, magnetic modeling has been viewed from two complementary perspectives: a microscopic one based on discrete dipoles and a macroscopic one based on continuous fields. By associating the former with particles and the latter with grids, the MPM framework of Sun et al. [SNZ*21] effectively bridges these two perspectives, revealing a coherent theoretical foundation that unites discrete and continuum views of magnetism. A lump of magnetic clay that is simulated by this framework is shown in Fig. 23.

## 5.3. Ferrofluids

Ferrofluids (also known as magnetic fluids) are colloidal suspensions of nanoscale ferromagnetic particles, which have found wide applications in materials science [LKC*19; ZSYZ19], robotics

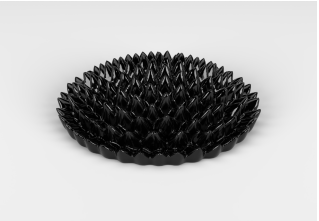

**(a)** *Normal-field instability;*

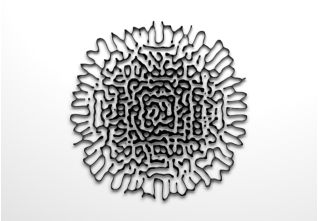

**(b)** *Labyrinthine instability.*

**Figure 24:** *Characteristic phenomena of ferrofluids. The normal-field instability arises due to the interplay of magnetic, gravitational, and capillary forces, leading to the formation of regular patterns or spikes aligned parallel to the magnetic field direction. The labyrinthine instability occurs when a thin layer of circular ferrofluid is sandwiched between two glass panes, and the magnetic field is applied perpendicular to the panes. Source: Ni et al. [NWWC24].*

[FDK*20; FJL*22], and artistic design [Kod08; YCE*16]. Due to the complex interplay of three distinct forces—gravity, magnetic forces, and surface tension—ferrofluids can form characteristic patterns, which, depending on their morphology, are referred to as normal-field instabilities and labyrinthine instabilities [Ros97]. See Fig. 24 for illustration.

Despite the name, ferrofluids do not exhibit macroscopic ferromagnetism. From a statistical mechanics perspective, Rosensweig [Ros97] described their magnetization using Langevin paramagnetism (see Eq. (12)). The fluid dynamics governing ferrofluids, based on the Navier–Stokes equations, are among the most complex, and consequently, the number of simulation frameworks developed for fluids is the largest. Across various frameworks, previous studies have successfully demonstrated the ability to reproduce ferrofluid instabilities in virtual environments.

#### 5.3.1. SPH Frameworks

In §4.2.1, we have introduced an SPH-based discretization and the corresponding magnetic field solver. Naturally, this approach finds its main use in SPH-based ferrofluid simulations. Because the SPH method smooths out the ferrofluid boundary, the magnetic pressure term on the surface vanishes, leaving only the problem of determining how to define and integrate the volumetric magnetic force density.

Huang et al. [HHM19] (see Fig. 25) constructed a ferrofluid simulation framework based on the Kelvin force (Eq. (22)) combined with the standard weakly incompressible SPH formulation augmented by artificial surface tension (see the tutorial by Koschier et al. [KBST22]). Since the magnetic field $\boldsymbol{B}$ (and hence $\boldsymbol{H}$ and $\boldsymbol{M}$, given a predefined susceptibility $\chi$) is already obtained by solving a linear system at each SPH particle center, directly evaluating the force density $f_\mathrm{m} = \mu_0(\boldsymbol{M}\cdot\nabla)\boldsymbol{H}$ at these centers is straightforward. However, this value cannot simply be treated as the uniform force density for the entire SPH particle, as SPH particles typically occupy a relatively large volume.

To address this issue, Huang et al. [HHM19] examined the

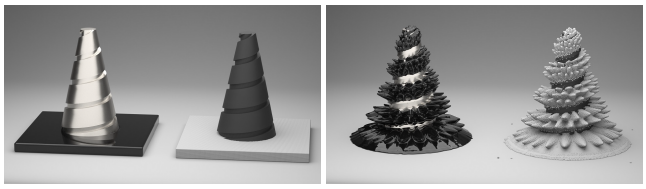

**Figure 25:** *Ferrofluid climbing up a magnetized helix. The helix mesh and SPH particles are visualized in parallel with the rendered ferrofluid. Source: Huang et al. [HHM19].*

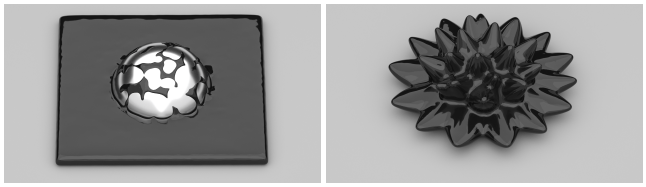

**Figure 26:** *Under magnetic actuation, the rest fluid evolves into a spiked equilibrium shape. Source: Shao et al. [SHM23].*

Kelvin force exerted by the $j$-th SPH particle on the $i$-th particle, expressed as

$$\begin{aligned}\boldsymbol{f}_{j\to i} &= \mu_0 \iiint_{V_i} \boldsymbol{M}_i(\boldsymbol{x})\cdot\nabla\boldsymbol{\eta}(\boldsymbol{x}-\boldsymbol{x}_j,\boldsymbol{m}_j)\,\mathrm{d}V_i \\ &= \mu_0\boldsymbol{m}_i\cdot\iiint_{V_i} W(\boldsymbol{x}-\boldsymbol{x}_i,h)\,\nabla\boldsymbol{\eta}(\boldsymbol{x}-\boldsymbol{x}_j,\boldsymbol{m}_j)\,\mathrm{d}V_i. \end{aligned} \tag{80}$$

When $\|\boldsymbol{x}_i-\boldsymbol{x}_j\|\geq 4h$, this integral admits an analytical solution:

$$\boldsymbol{f}_{j\to i} = \mu_0(\boldsymbol{m}_i\cdot\nabla)\boldsymbol{\eta}(\boldsymbol{x}_i-\boldsymbol{x}_j,\boldsymbol{m}_j), \tag{81}$$

which coincides with the force exerted by magnetic moment $\boldsymbol{m}_j$ on magnetic moment $\boldsymbol{m}_i$. However, when $\|\boldsymbol{x}_i-\boldsymbol{x}_j\|<4h$, we must numerically integrate Eq. (80).

Since performing such numerical integration for every pair of SPH particles is prohibitively expensive, Huang et al. [HHM19] instead precomputed the integral for a range of particle distances $\|\boldsymbol{x}_i-\boldsymbol{x}_j\|$, kernel radii $h$, and moment orientations $(\boldsymbol{m}_i,\boldsymbol{m}_j)$, and then fitted the results using piecewise polynomial functions for efficient runtime evaluation—essentially constructing a lookup table. Because there are $O(N^2)$ such pairwise interactions among $N$ SPH particles, they further modified the fast multipole method to accelerate the summation of these forces in this specific formulation.

**Divergence-free SPH.** Shao et al. [SHM23] extended the above framework to Divergence-Free SPH (DFSPH) [BK15], by which the results are shown in Fig. 26. They observed that incorporating the Kelvin force into DFSPH led to poor convergence, primarily because it can yield outward-pointing forces, especially near the ferrofluid surface. This tends to spuriously expand the fluid volume and thus undermines the incompressibility constraints. To overcome this issue, they adopted the *current-loop force model* [Byr77] instead of the Kelvin force model, defined as

$$f_\mathrm{m} = (\boldsymbol{M}\cdot\nabla)\boldsymbol{B} = \mu_0(\boldsymbol{M}\cdot\nabla)\boldsymbol{H} + \mu_0(\boldsymbol{M}\cdot\nabla)\boldsymbol{M}. \tag{82}$$

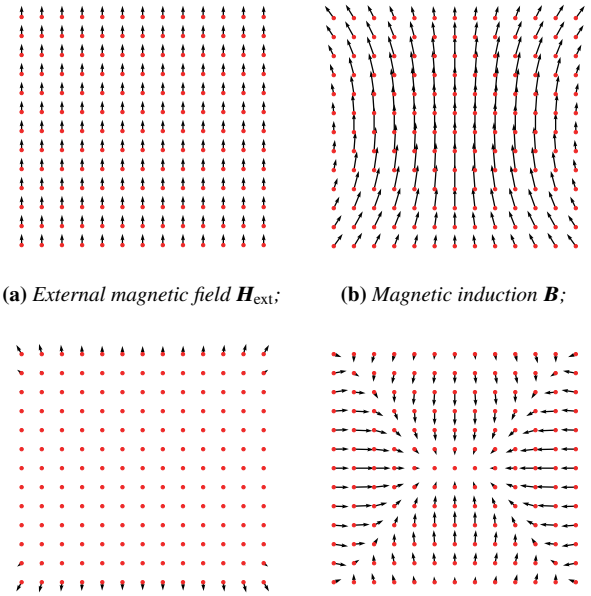

**(a)** *External magnetic field* $\boldsymbol{H}_{\text{ext}}$; **(b)** *Magnetic induction* $\boldsymbol{B}$; **(c)** *Kelvin force;* **(d)** *Current loop force.*

**Figure 27:** *Illustration of the Kelvin and current loop force models in a uniform external magnetic field. The Kelvin force points outward, while the current loop force points inward. Source: Shao et al. [SHM23].*

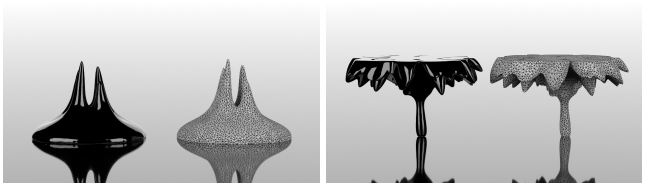

**Figure 28:** *Ferrofluid on the ground being attracted by an upper magnet. The underlying surface mesh is visualized. Source: Huang and Michels [HM20].*

The first term corresponds to the Kelvin force term, and the second term can be expressed as

$$\frac{\mu_0}{2}\|\boldsymbol{M}\|^2 - \mu_0 \boldsymbol{M} \times (\nabla \times \boldsymbol{M}). \tag{83}$$

Intuitively, $\|\boldsymbol{M}\|^2$ is larger inside the ferrofluid and vanishes outside, so this additional term promotes inward-pointing forces near the interface. This difference in the resulting force directions is illustrated in Fig. 27. From a continuum viewpoint, the Kelvin and current loop forms yield the same interfacial traction. Their difference can be absorbed into the pressure in an incompressible formulation. Introducing this term alleviates the spurious expansion and makes the simulation more compatible with the DFSPH framework. The evaluation approach for this current-loop force follows exactly the same strategy as Huang et al. [HHM19] used for the Kelvin force.

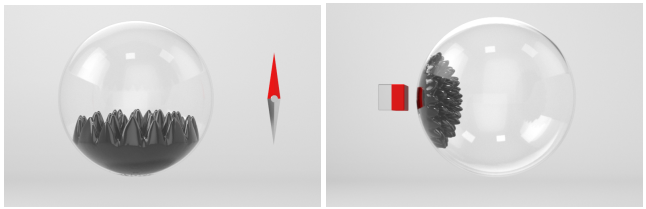

**Figure 29:** *Ferrofluid inside a crystal ball magnetized by an external magnetic field (left) and a magnet (right). Source: Ni et al. [NZWC20].*

#### 5.3.2. Surface-Only Frameworks

Da et al. [DHB*16] proposed a surface-only liquid simulation framework, which assumes that the fluid velocity field $\boldsymbol{u}$ is harmonic ($\nabla \times \boldsymbol{u} = \boldsymbol{0}$ and $\nabla \cdot \boldsymbol{u} = 0$). Under this assumption, the velocity on the boundary alone suffices to represent the entire flow field. Consequently, the method requires no volumetric discretization. Maintaining only the surface mesh is sufficient for performing the simulation.

Surface-based fluid simulation offers two major advantages. First, the explicit representation of the surface naturally ensures excellent volume preservation. Second, the mean curvature required for computing surface tension can be directly obtained using discrete differential geometry techniques (see the book of Botsch et al. [BKP*10]), achieving high accuracy. For ferrofluid simulations, where surface tension plays a critical role, this explicit surface representation also facilitates the use of BEMs for solving the magnetic field (§4.2.3).

Huang et al. [HM20] adopted a Galerkin BEM formulation with double-layer potentials as their magnetostatic solver, and used the computed $\boldsymbol{H}$-field to evaluate the magnetic pressure (Eq. (74)), which is later integrated into the surface-only pressure solver. Such a ferrofluid simulation pipeline required minimal modification to the original surface-only liquid framework but is sensitive to the accuracy of numerical integration, as pointed out by Huang and Michels [HM20]. According to their ablation studies, employing a low-order BEM scheme (such as the collocation method) led to increased energy dissipation, while computing magnetic pressure only at vertices, rather than integrating it over faces using quadrature points, often caused simulation instabilities or crashes. They further observed that only the double-layer potential formulation was stable in the surface-only context. Using a single-layer potential under the same numerical setup likewise resulted in crashes.

We demonstrate the surface-only ferrofluid simulation in Fig. 28.

#### 5.3.3. Grid-Based Frameworks

Grid-based (Eulerian) fluid simulation [Bri15] typically employs the level-set method [OF03] for tracking free surfaces. In this formulation, the interface is implicitly represented by a signed distance field (SDF) $\varphi(\boldsymbol{x})$, which is advected with the flow and periodically reinitialized to maintain numerical stability. Geometric quantities on the surface, such as the outward normal and mean curvature, can be directly computed as $\boldsymbol{n} = \nabla\varphi/\|\nabla\varphi\|$ and $\kappa = \nabla \cdot \boldsymbol{n}$,

respectively. Consequently, the surface tension at any surface point can be readily evaluated via Eq. (37).

Within the grid-based simulation framework, *pressure projection* constitutes the core step. It solves for the pressure field $p$ under a finite-difference discretization and uses the pressure gradient force $-\nabla p$ to project the velocity field $\boldsymbol{u}$ onto a divergence-free space, enforcing incompressibility. Since surface tension can be expressed as a pressure jump across the interface (Eq. 37), it naturally appears as a boundary condition in the pressure projection step. This treatment of surface tension is known as the *ghost fluid method (GFM)* [KFL00; GFCK02], which enforces interfacial discontinuities in a sharp yet numerically stable manner.

As discussed in §5.1.2, the magnetic force derived from $\boldsymbol{T}_\mathrm{m}$ in Minkowski formulation can be interpreted as an effective pressure difference across the boundary. Therefore, we can incorporate the magnetic contribution into the conventional capillary pressure $p_\mathrm{c} = 2\gamma\kappa$ to obtain a magnetically augmented surface tension model:

$$\Delta p = p - p_\mathrm{air} = p_\mathrm{c} - p_\mathrm{m}. \tag{84}$$

By enforcing this condition as the boundary constraint in the pressure projection step, we can simulate the dynamics of ferrofluids. As in §5.1.2, both FDM and BEM are available for determining the magnetic field. Since grid-based fluid simulations typically use level sets to track the fluid interface, FDM can directly reuse the level-set function $\varphi$ without additional preprocessing [NZWC20]. The simulation results are given in Fig. 29.

When coupling grid-based fluid solvers with a BEM-based magnetostatic solver, Ni et al. [NWWC24] observed that the surface mesh extracted from the level-set function $\varphi$ using marching cubes [LC87] is particularly well suited as the input for BEM, owing to several essential properties:

- It is fine-grained that the distance between neighbouring vertices is less than $\sqrt{3}\Delta x$;
- Its vertex positions $\{\boldsymbol{x}_i\}$ align precisely with all the interface points required for evaluation in the ghost fluid method;
- Local vertex areas $\{\Delta A_i\}$ can be readily determined based on its topological characteristics.

Here, the local vertex area $\Delta A_i$ is estimated as one-third of the total area of all adjacent faces connected to the vertex. Therefore, Ni et al. [NWWC24] adopted fixed-point iterations to solve the BEM based on the single-layer potential (§4.2.3), and integrates the resulting magnetic pressure into the grid-based fluid solver as they did for FDM. See Fig. 24 for results.

It is worth noting that the inherent non-conservative nature of level-set methods becomes more pronounced when applied to ferrofluid simulations. Existing work [NZWC20; NWWC24] addresses this issue by incorporating a volume control strategy [KLL*07] during the projection step, effectively compensating for volume gain or loss through artificial adjustment.

## 6. Discussions

At present, research on magnetic modeling and simulation in computer graphics can be broadly categorized into two paradigms. The first approximates magnetization and magnetic forces through the interactions among discrete dipoles, typically applied to magnetic solids. The second solves for continuous magnetic fields within the medium using various numerical methods, primarily targeting magnetic fluids. In terms of computational efficiency, the former offers a clear advantage; in terms of physical fidelity, the latter provides a more accurate and principled description of magnetism. Much like the coexistence of sphere-based approximations and incremental potential contact models in collision handling, or mass–spring systems and finite element methods in cloth simulation, both paradigms serve distinct purposes and remain valuable directions for continued exploration.

Overall, computer graphics researchers have achieved remarkable progress in physics-based animation of magnetic materials, spanning rigid bodies, elastic solids, and fluids, as well as both linear and nonlinear magnetization behaviors. These efforts have produced numerous visually convincing and aesthetically appealing results, contributing substantially to the advancement of digital content creation. Nevertheless, current magnetostatic solvers and magnetic material simulation pipelines still face several common challenges and inherent limitations. In the following, we summarize these issues and discuss potential directions for future research, hoping to inspire further development in this exciting domain.

**Implicit schemes.** Magnetic fields are determined by the instantaneous configuration of the material. Consequently, any numerical scheme that first evaluates the magnetic field and magnetic forces based on the current state and then integrates forward in time to obtain the next state is explicit in nature. From this perspective, among all the frameworks discussed in this paper, only the differentiable magnetic shells proposed by Chen et al. [CNZ*22] employ a fully implicit time integration scheme, though their formulation is limited to hard-magnetic materials. Similarly, the semi-implicit framework by Westhofen et al. [WFJB24] also treats all magnetic components as permanent magnets during per-step energy optimization. To date, there exists no numerical formulation that implicitly computes magnetic forces based on the future configuration while accounting for linear or nonlinear magnetization. In computer graphics, implicit integration methods are known to significantly improve the stability and computational efficiency of dynamic simulations. Making progress in this direction could therefore play a pivotal role in bringing magnetic modeling and simulation into real-time 3D applications.

**Nonlinear magnetization.** In physics, understanding the mechanisms underlying magnetization has been fundamental to major developments throughout the 20th century. In computer graphics, however, most existing methods are built upon the assumption of linear magnetization, an approximation that holds only under restrictive physical conditions and is therefore of limited applicability in practice. Although Kim et al. [KPH18] approached nonlinear magnetization from a micromagnetic perspective and Sun et al. [SNZ*21] modeled it using Langevin paramagnetism, both attempts remain relatively coarse and suffer from clear numerical limitations: the magnetization dynamics of Kim et al. [KPH18] are primarily qualitative and constrained to rigid bodies, while the method of Sun et al. [SNZ*21] requires Newton iterations over the entire grid, resulting in significant computational overhead. A promising research direction might be to address nonlinear magnetization within the framework of BEMs. This would, however,

demand new theoretical developments, since interior terms such as $\nabla \cdot \boldsymbol{M}$ generally introduce volume contributions and thus cannot be represented only using boundary integrals. That is why all boundary integral equations presented in §4.2.3 assume linear magnetization. Furthermore, well-established physical models, such as the Ising model of ferromagnetic phase transitions [Isi25; Ons44] and the Jiles–Atherton hysteresis model [JA86], possess corresponding numerical formulations but have yet to be explored in computer graphics applications.

**Differentiable solvers.** A defining feature of magnetic materials is their long-range controllability, which grants them decisive importance in fields such as biomedicine and robotics. To promote deeper integration between numerical tools in computer graphics and these application domains, it is not sufficient to perform accurate and efficient forward modeling and simulation. We must also enable inverse optimization, which demands that the solvers themselves be differentiable. At present, only the work of Chen et al. [CNZ*22] has explicitly addressed this requirement, successfully reproducing laboratory experiments [ZKC*19] within a virtual environment. In the biomedical context, Yan et al. [YSS*24] leveraged magnetic modeling techniques from graphics to design and analyze their soft microrobots. However, the potential of such digital-twin-based approaches remains far from fully realized. In this regard, boundary-integral formulations under BEM offer a critical advantage by reducing volumetric DoFs to surface samples. While the resulting long-range interactions are dense, they can be efficiently accelerated using FMM, which yields linear computational complexity. Equipping such scalable FMM or BEM pipelines with differentiability would enable real-time or near-real-time simulation of extremely large-scale magnetic systems containing millions of dipoles. This capability would empower engineers to interactively test and refine complex assemblies composed of numerous microscopic magnets (such as magnetic bearings or robotic swarms), thereby enabling rapid validation of their kinematic and dynamic performance and dramatically accelerating the design cycle.

**Integration into PIC/FLIP.** While previous studies have successfully extended various popular fluid simulation frameworks, such as SPH, surface-only, and grid-based methods, to support magnetic fluids, one of the most prominent framework in modern computer graphics, PIC/FLIP [ZB05], has yet to receive similar attention. Compared with the aforementioned methods, PIC/FLIP offers superior conservation of volume [KLTB21], linear momentum, and angular momentum [JSS*15]. However, it suffers from a critical drawback in the context of magnetic fluid simulation: the difficulty of applying surface tension. This issue has been noted by Sun et al. [SNZ*21], who, for this very reason, were unable to extend their MPM framework to ferrofluid simulation. One possible workaround is to adopt a two-phase FLIP formulation, as in MultiFLIP [BB12], to better preserve the liquid–air interface, which introduces additional overhead. More recently, Hyde et al. [HGMT20] formulated surface tension from a surface-energy objective and discretized its forces within MPM, which could potentially be adapted to other hybrid solvers. Another straightforward solution may be to borrow ideas from SPH and introduce an artificial surface tension term [JWL*23] to approximate curvature-based effects. Other possible directions include adapting PIC/FLIP in a manner similar to MPM to improve its magnetic compatibility, enabling both particles and grids to jointly represent magnetic field and magnetization information. In addition, recent advances in using the lattice Boltzmann method (LBM) [MXL*24] for water simulation have shown impressive results in graphics [LMLD22]. Integrating magnetic effects into such highly parallel solvers could lead to large-scale, efficient magnetic fluid simulations.

**Human–computer interaction.** Magnetic materials are transforming next-generation robotics by enabling non-contact actuation and complex deformations [KPLZ19; HLMS18; EM13], while simultaneously providing proprioception and high-precision tactile sensing via magnetoelastic and inductive effects [ZZX*24; KLS*14]. As a breakthrough "electronic skin" technology, magnetic tactile sensing converts physical contact into digital signals [ZCJC24; MCC22; KZ22] with exceptional robustness, accuracy, and multimodal capability—effectively bridging the physical and digital worlds. The frontier of this research field lies in the paradigm of "Hardware-Defined Sensing." Its efficacy stems from customized magnetic encoding—utilizing multi-pole arrays and structured laminates to transfigure complex mechanical motions into spatially unique magnetic signatures. This architecture facilitates the physical pre-encoding of mechanical DoFs, embedding sensing intelligence into the material morphology. Magnetic modeling and simulation underpin this process, providing the foundation for signal capture, recognition, and interpretation, and enabling a high-fidelity, real-time tactile digital twin that bridges hardware-defined magnetic encoding with algorithmic inference. A primary challenge is the physical decoupling of forces and torques through the coordinated design of magnetization patterns and sensor structures [DZP*24], allowing robots to extract structured mechanical information from complex contacts. Here, simulation-driven morphological optimization quantifies the spatial orthogonality and field gradients of diverse magnetic patterns, ensuring that each mechanical DoF produces a distinct "magnetic fingerprint" that maximizes decoupling resolution at the source. This capability facilitates the understanding of fundamental interaction modes—pushing, pulling, twisting, and sliding—supporting precise manipulation, safe interaction, and natural human–robot interfaces. Another challenge lies in handling the nonlinear, time-varying nature of tactile signals arising from the fundamental physics of contact. Future research must develop real-time magnetic simulation frameworks capable of dynamically reconstructing multidimensional force and torque data [YHY*21; YSSP22] under strict computational constraints, where reduced-order or neural surrogate models trained on synthetic simulation data enable fast inverse mapping from composite magnetic signals to decoupled force and torque components. Such physics-based models will enable synchronized virtual-real perception and advance innovation in robotics, virtual reality, and human-machine collaboration.

## 7. Conclusion

This survey presents a systematic review of magnetic modeling and simulation, a topic that has recently gained increasing attention in the computer graphics community. As the first comprehensive survey dedicated to this area, it aims to clarify the distinctions and

connections among existing studies in terms of their physical formulations and numerical solvers. All these methods originate from the same underlying magnetostatic principles and equations of motion, yet adapt to graphics applications through varying degrees of approximation and discretization.

We have provided an organized summary of the methods' respective strengths and limitations, highlighting the diverse strategies that have emerged across various magnetic materials. We hope this paper, by consolidating fragmented knowledge into a unified framework, can serve as both an introductory reference for practitioners entering the field of magnetic modeling and simulation, and a guidepost for researchers seeking promising future directions—fostering both the practical adoption and academic advancement of this emerging topic in computer graphics.

## References


[ADW97] ABOU, BERENGERE, DE SURGY, G NÉRON, and WESFREID, JOSE-EDUARDO. "Dispersion relation in a ferrofluid layer of any thickness and viscosity in a normal magnetic field; asymptotic regimes". *Journal de Physique II* 7.8 (1997), 1159–1171. DOI: 10.1051/jp2:1997178 23.

[AEF22] ANDREWS, SHELDON, ERLEBEN, KENNY, and FERGUSON, ZACHARY. "Contact and friction simulation for computer graphics". *ACM SIGGRAPH 2022 Courses*. SIGGRAPH '22. Vancouver, British Columbia, Canada: Association for Computing Machinery, 2022. DOI: 10.1145/3532720.3535640 13.

[AFM*22] ANGHINONI, B., FLIZIKOWSKI, G.A.S., MALACARNE, L.C., et al. "On the formulations of the electromagnetic stress–energy tensor". *Annals of Physics* 443 (2022), 169004. ISSN: 0003-4916. DOI: 10.1016/j.aop.2022.169004 5.

[Bat00] BATCHELOR, GEORGE K. *An Introduction to Fluid Dynamics*. Cambridgeshire, England, UK: Cambridge University Press, 2000. DOI: 10.1017/CBO9780511800955 6.

[BB12] BOYD, LANDON and BRIDSON, ROBERT. "MultiFLIP for energetic two-phase fluid simulation". *ACM Trans. Graph.* 31.2 (Apr. 2012). DOI: 10.1145/2159516.2159522 19.

[BFA02] BRIDSON, ROBERT, FEDKIW, RONALD, and ANDERSON, JOHN. "Robust treatment of collisions, contact and friction for cloth animation". *ACM Trans. Graph.* 21.3 (July 2002), 594–603. DOI: 10.1145/566654.566623 2.

[BG97] BEATSON, RICK and GREENGARD, LESLIE. "A short course on fast multipole methods". *Wavelets, Multilevel Methods and Elliptic PDEs*. New York, NY, USA: Oxford University Press, 1997, 1–37 9.

[BK15] BENDER, JAN and KOSCHIER, DAN. "Divergence-free smoothed particle hydrodynamics". *Proceedings of the 14th ACM SIGGRAPH / Eurographics Symposium on Computer Animation*. SCA '15. Los Angeles, California: Association for Computing Machinery, 2015, 147–155. DOI: 10.1145/2786784.2786796 16.

[BKP*10] BOTSCH, BYMARIO, KOBBELT, LEIF, PAULY, MARK, et al. *Polygon Mesh Processing*. 1st. Boca Raton, FL, USA: A K Peters/CRC Press, 2010. DOI: 10.1201/b10688 17.

[Bri15] BRIDSON, ROBERT. *Fluid simulation for computer graphics*. 2nd. Boca Raton, FL, USA: A K Peters/CRC Press, 2015. DOI: 10.1201/9781315266008 17.

[BW98] BARAFF, DAVID and WITKIN, ANDREW. "Large steps in cloth simulation". *Proceedings of the 25th Annual Conference on Computer Graphics and Interactive Techniques*. SIGGRAPH '98. New York, NY, USA: Association for Computing Machinery, 1998, 43–54. DOI: 10.1145/280814.280821 2.

[Byr77] BYRNE, JAMES V. "Ferrofluid hydrostatics according to classical and recent theories of the stresses". *Proceedings of the Institution of Electrical Engineers*. Vol. 124. 11. IET. 1977, 1089–1097 16.

[CNZ*22] CHEN, XUWEN, NI, XINGYU, ZHU, BO, et al. "Simulation and optimization of magnetoelastic thin shells". *ACM Trans. Graph.* 41.4 (July 2022). DOI: 10.1145/3528223.3530142 1, 2, 7, 15, 18, 19.

[Cou15] COUMANS, ERWIN. "Bullet physics simulation". *ACM SIGGRAPH 2015 Courses*. SIGGRAPH '15. Los Angeles, California: Association for Computing Machinery, 2015. DOI: 10.1145/2776880.2792704 13.

[CR67] COWLEY, MD and ROSENSWEIG, RONALD E. "The interfacial stability of a ferromagnetic fluid". *Journal of Fluid mechanics* 30.4 (1967), 671–688. DOI: 10.1017/S0022112067001697 23.

[DHB*16] DA, FANG, HAHN, DAVID, BATTY, CHRISTOPHER, et al. "Surface-only liquids". *ACM Trans. Graph.* 35.4 (July 2016). DOI: 10.1145/2897824.2925899 2, 17.

[DZP*24] DAI, HUANGZHE, ZHANG, CHENGQIAN, PAN, CHENGFENG, et al. "Split-Type Magnetic Soft Tactile Sensor with 3D Force Decoupling". *Advanced Materials* 36.11 (2024), 2310145. DOI: 10.1002/adma.202310145 19.

[EL08] EINSTEIN, ALBERT and LAUB, JAKOB. "Über die im elektromagnetischen Felde auf ruhende Körper ausgeübten ponderomotorischen Kräfte". *Annalen der Physik* 331.8 (1908), 541–550. DOI: 10.1002/andp.19083310807 5.

[EM13] ERIC, DILLER and METIN, SITTI. *Micro-Scale Mobile Robotics*. Hanover, MA, USA: Now Foundations and Trends, 2013. DOI: 10.1561/2300000023 19.

[FAMO99] FEDKIW, RONALD P., ASLAM, TARIQ, MERRIMAN, BARRY, and OSHER, STANLEY. "A Non-oscillatory Eulerian Approach to Interfaces in Multimaterial Flows (the Ghost Fluid Method)". *Journal of Computational Physics* 152.2 (1999), 457–492. DOI: 10.1006/jcph.1999.6236 2.

[FDK*20] FAN, XINJIAN, DONG, XIAOGUANG, KARACAKOL, ALP C., et al. "Reconfigurable multifunctional ferrofluid droplet robots". *Proceedings of the National Academy of Sciences* 117.45 (2020), 27916–27926. DOI: 10.1073/pnas.2016388117 16.

[FJL*22] FAN, XINJIAN, JIANG, YIHUI, LI, MINGTONG, et al. "Scale-reconfigurable miniature ferrofluidic robots for negotiating sharply variable spaces". *Science Advances* 8.37 (2022), eabq1677. DOI: 10.1126/sciadv.abq1677 16.

[FLS*21] FERGUSON, ZACHARY, LI, MINCHEN, SCHNEIDER, TESEO, et al. "Intersection-free rigid body dynamics". *ACM Trans. Graph.* 40.4 (July 2021). DOI: 10.1145/3450626.3459802 13.

[FSJ01] FEDKIW, RONALD, STAM, JOS, and JENSEN, HENRIK WANN. "Visual simulation of smoke". *Proceedings of the 28th Annual Conference on Computer Graphics and Interactive Techniques*. SIGGRAPH '01. New York, NY, USA: Association for Computing Machinery, 2001, 15–22. DOI: 10.1145/383259.383260 2.

[GFCK02] GIBOU, FREDERIC, FEDKIW, RONALD P., CHENG, LI-TIEN, and KANG, MYUNGJOO. "A Second-Order-Accurate Symmetric Discretization of the Poisson Equation on Irregular Domains". *Journal of Computational Physics* 176.1 (2002), 205–227. DOI: 10.1006/jcph.2001.6977 18.

[Gri23] GRIFFITHS, DAVID J. *Introduction to Electrodynamics*. 5th ed. Cambridgeshire, England, UK: Cambridge University Press, 2023. DOI: 10.1017/9781009397735 2.

[HGMT20] HYDE, DAVID A. B., GAGNIERE, STEVEN W., MARQUEZ-RAZON, ALAN, and TERAN, JOSEPH. "An implicit updated lagrangian formulation for liquids with large surface energy". *ACM Trans. Graph.* 39.6 (Nov. 2020). DOI: 10.1145/3414685.3417845 19.

[HHM19] HUANG, LIBO, HÄDRICH, TORSTEN, and MICHELS, DOMINIK L. "On the accurate large-scale simulation of ferrofluids". *ACM Trans. Graph.* 38.4 (July 2019). DOI: 10.1145/3306346.3322973 1, 2, 9, 10, 16, 17.

[HLMS18] HU, WENQI, LUM, GUO ZHAN, MASTRANGELI, MASSIMO, and SITTI, METIN. "Small-scale soft-bodied robot with multimodal locomotion". *Nature* 554 (2018), 81–85. DOI: 10.1038/nature25443 19.

[HM20] HUANG, LIBO and MICHELS, DOMINIK L. "Surface-only ferrofluids". *ACM Trans. Graph.* 39.6 (Nov. 2020). DOI: 10.1145/3414685.3417799 2, 10–12, 17.

[Hou13] HOUDE HAN, XIAONAN WU. *Artificial Boundary Method*. Berlin, Heidelberg: Springer, 2013. DOI: 10.1007/978-3-642-35464-9 11.

[HW65] HARLOW, FRANCIS H. and WELCH, J. EDDIE. "Numerical calculation of time-dependent viscous incompressible flow of fluid with free surface". *The Physics of Fluids* 8.12 (1965), 2182–2189. DOI: 10.1063/1.1761178 10.

[Isi25] ISING, ERNST. "Beitrag zur Theorie des Ferromagnetismus". *Zeitschrift für Physik* 31.1 (1925), 253–258. DOI: 10.1007/BF02980577 19.

[IYI*13] ISHIKAWA, TOMOKAZU, YUE, YONGHAO, IWASAKI, KEI, et al. "Visual Simulation of Magnetic Fluid Using a Procedural Approach for Spikes Shape". *Computer Vision, Imaging and Computer Graphics. Theory and Application*. Ed. by CSURKA, GABRIELA, KRAUS, MARTIN, LARAMEE, ROBERT S., et al. Berlin, Heidelberg: Springer Berlin Heidelberg, 2013, 112–126. DOI: 10.1007/978-3-642-38241-3_8 2.

[JA86] JILES, D.C. and ATHERTON, D.L. "Theory of ferromagnetic hysteresis". *Journal of Magnetism and Magnetic Materials* 61.1 (1986), 48–60. DOI: 10.1016/0304-8853(86)90066-1 19.

[Jac98] JACKSON, JOHN DAVID. *Classical Electrodynamics*. 3rd ed. New York, NY, USA: John Wiley & Sons, 1998 2, 14.

[JSS*15] JIANG, CHENFANFU, SCHROEDER, CRAIG, SELLE, ANDREW, et al. "The affine particle-in-cell method". *ACM Trans. Graph.* 34.4 (July 2015). DOI: 10.1145/2766996 19.

[JST*16] JIANG, CHENFANFU, SCHROEDER, CRAIG, TERAN, JOSEPH, et al. "The material point method for simulating continuum materials". *ACM SIGGRAPH 2016 Courses*. SIGGRAPH '16. Anaheim, California: Association for Computing Machinery, 2016. DOI: 10.1145/2897826.2927348 14.

[JWL*23] JESKE, STEFAN RHYS, WESTHOFEN, LUKAS, LÖSCHNER, FABIAN, et al. "Implicit Surface Tension for SPH Fluid Simulation". *ACM Trans. Graph.* 43.1 (Nov. 2023). DOI: 10.1145/3631936 19.

[KBST22] KOSCHIER, DAN, BENDER, JAN, SOLENTHALER, BARBARA, and TESCHNER, MATTHIAS. "A Survey on SPH Methods in Computer Graphics". *Computer Graphics Forum* 41.2 (2022), 737–760. DOI: 10.1111/cgf.14508 16.

[KFL00] KANG, MYUNGJOO, FEDKIW, RONALD P., and LIU, XU-DONG. "A Boundary Condition Capturing Method for Multiphase Incompressible Flow". *Journal of Scientific Computing* 15.3 (2000), 323–360. DOI: 10.1023/A:1011178417620 18.

[KH20] KIM, SEUNG-WOOK and HAN, JUNGHYUN. "Simulation of Arbitrarily-shaped Magnetic Objects". *Computer Graphics Forum* 39.7 (2020), 119–130. DOI: 10.1111/cgf.14131 1, 2, 8, 12–14.

[KH22] KIM, SEUNG-WOOK and HAN, JUNGHYUN. "Fast Stabilization of Inducible Magnet Simulation". *SIGGRAPH Asia 2022 Conference Papers*. SA '22. Daegu, Republic of Korea: Association for Computing Machinery, 2022. DOI: 10.1145/3550469.3555410 1, 2, 8, 9, 13.

[KLL*07] KIM, BYUNGMOON, LIU, YINGJIE, LLAMAS, IGNACIO, et al. "Simulation of bubbles in foam with the volume control method". *ACM Trans. Graph.* 26.3 (July 2007), 98–es. DOI: 10.1145/1276377.1276500 18.

[KLS*14] KIM, JAEMIN, LEE, MINCHEOL, SHIM, HYUNG JOON, et al. "Stretchable silicon nanoribbon electronics for skin prosthesis". *Nature communications* 5 (Dec. 2014), 5747. DOI: 10.1038/ncomms6747 19.

[KLTB21] KUGELSTADT, TASSILO, LONGVA, ANDREAS, THUEREY, NILS, and BENDER, JAN. "Implicit Density Projection for Volume Conserving Liquids". *IEEE Transactions on Visualization and Computer Graphics* 27.4 (2021), 2385–2395. DOI: 10.1109/TVCG.2019.2947437 19.

[Kod08] KODAMA, SACHIKO. "Dynamic ferrofluid sculpture: organic shape-changing art forms". *Commun. ACM* 51.6 (June 2008), 79–81. DOI: 10.1145/1349026.1349042 16.

[KPH18] KIM, SEUNG-WOOK, PARK, SUN YOUNG, and HAN, JUNGHYUN. "Magnetization dynamics for magnetic object interactions". *ACM Trans. Graph.* 37.4 (July 2018). DOI: 10.1145/3197517.3201402 2, 8, 12, 13, 18.

[KPLZ19] KIM, YOONHO, PARADA, GERMAN A., LIU, SHENGDUO, and ZHAO, XUANHE. "Ferromagnetic soft continuum robots". *Science Robotics* 4.33 (2019), eaax7329. DOI: 10.1126/scirobotics.aax7329 15, 19.

[KZ22] KIM, YOONHO and ZHAO, XUANHE. "Magnetic Soft Materials and Robots". *Chemical Reviews* 122.5 (2022), 5317–5364. DOI: 10.1021/acs.chemrev.1c00481 19.

[Lan05] LANGEVIN, PAUL. "Sur la théorie du magnétisme". *Journal de Physique Théorique et Appliquée* 4.1 (1905), 678–693. DOI: 10.1051/jphystap:019050040067800 3, 4.

[LC87] LORENSEN, WILLIAM E. and CLINE, HARVEY E. "Marching Cubes: A High Resolution 3D Surface Construction Algorithm". *SIGGRAPH Comput. Graph.* 21.4 (Aug. 1987), 163–169. DOI: 10.1145/37402.37422 12, 18.

[LFS*20] LI, MINCHEN, FERGUSON, ZACHARY, SCHNEIDER, TESEO, et al. "Incremental potential contact: intersection-and inversion-free, large-deformation dynamics". *ACM Trans. Graph.* 39.4 (Aug. 2020). DOI: 10.1145/3386569.3392425 2.

[LKC*19] LIU, XUBO, KENT, NOAH, CEBALLOS, ALEJANDRO, et al. "Reconfigurable ferromagnetic liquid droplets". *Science* 365.6450 (2019), 264–267. DOI: 10.1126/science.aaw8719 15.

[LMLD22] LI, WEI, MA, YIHUI, LIU, XIAOPEI, and DESBRUN, MATHIEU. "Efficient kinetic simulation of two-phase flows". *ACM Trans. Graph.* 41.4 (July 2022). DOI: 10.1145/3528223.3530132 19.

[MCC22] MAN, JIANDONG, CHEN, GUANGYUAN, and CHEN, JIAMIN. "Recent Progress of Biomimetic Tactile Sensing Technology Based on Magnetic Sensors". *Biosensors* 12.11 (2022). DOI: 10.3390/bios12111054 19.

[MCG03] MÜLLER, MATTHIAS, CHARYPAR, DAVID, and GROSS, MARKUS. "Particle-based fluid simulation for interactive applications". *Proceedings of the 2003 ACM SIGGRAPH/Eurographics Symposium on Computer Animation*. SCA '03. San Diego, California: Eurographics Association, 2003, 154–159. DOI: 10.5555/846276.846298 1.

[Min08] MINKOWSKI, HERMANN. "Die Grundgleichungen für die elektromagnetischen Vorgänge in bewegten Körpern". *Nachrichten von der Gesellschaft der Wissenschaften zu Göttingen, Mathematisch-Physikalische Klasse* 1908.1 (1908), 53–111. DOI: 10.1007/BF01455871 5.

[MST10] MCADAMS, A., SIFAKIS, E., and TERAN, J. "A Parallel Multigrid Poisson Solver for Fluids Simulation on Large Grids". *Proceedings of the 2010 ACM SIGGRAPH/Eurographics Symposium on Computer Animation*. SCA '10. Madrid, Spain: Eurographics Association, 2010, 65–74. DOI: 10.5555/1921427.1921438 10.

[MXL*24] MA, YIHUI, XIAO, XIAOYU, LI, WEI, et al. "Hybrid LBM-FVM solver for two-phase flow simulation". *Journal of Computational Physics* 506 (2024), 112920. DOI: 10.1016/j.jcp.2024.112920 19.

[NRC21] NABIZADEH, MOHAMMAD SINA, RAMAMOORTHI, RAVI, and CHERN, ALBERT. "Kelvin transformations for simulations on infinite domains". *ACM Trans. Graph.* 40.4 (July 2021). DOI: 10.1145/3450626.3459809 11.

[NWWC24] NI, XINGYU, WANG, RUICHENG, WANG, BIN, and CHEN, BAOQUAN. "An Induce-on-Boundary Magnetostatic Solver for Grid-Based Ferrofluids". *ACM Trans. Graph.* 43.4 (July 2024). DOI: 10.1145/3658124 1, 2, 10–14, 16, 18.

[NZWC20] NI, XINGYU, ZHU, BO, WANG, BIN, and CHEN, BAOQUAN. "A level-set method for magnetic substance simulation". *ACM Trans. Graph.* 39.4 (Aug. 2020). DOI: 10.1145/3386569.3392445 2, 6, 10, 12–14, 17, 18.

[OF03] OSHER, STANLEY and FEDKIW, RONALD P. *Level Set Methods and Dynamic Implicit Surfaces*. New York, NY, USA: Springer, 2003. DOI: 10.1007/b98879 17.

[Ons44] ONSAGER, LARS. "Crystal Statistics. I. A Two-Dimensional Model with an Order-Disorder Transition". *Phys. Rev.* 65.3-4 (Feb. 1944), 117–149. DOI: 10.1103/PhysRev.65.117 19.

[PKA*05] PAULY, MARK, KEISER, RICHARD, ADAMS, BART, et al. "Meshless animation of fracturing solids". *ACM Trans. Graph.* 24.3 (July 2005), 957–964. DOI: 10.1145/1073204.1073296 2.

[RGJ*15] RAM, DANIEL, GAST, THEODORE, JIANG, CHENFANFU, et al. "A material point method for viscoelastic fluids, foams and sponges". *Proceedings of the 14th ACM SIGGRAPH / Eurographics Symposium on Computer Animation*. SCA '15. Los Angeles, California: Association for Computing Machinery, 2015, 157–163. DOI: 10.1145/2786784.2786798 6.

[Ros97] ROSENSWEIG, RONALD E. *Ferrohydrodynamics*. Mineola, NY, USA: Dover Publications, Inc., 1997 16.

[RSG*08] ROBINSON-MOSHER, AVI, SHINAR, TAMAR, GRETARSSON, JON, et al. "Two-way coupling of fluids to rigid and deformable solids and shells". *ACM Trans. Graph.* 27.3 (Aug. 2008), 1–9. DOI: 10.1145/1360612.1360645 11.

[SB12] SIFAKIS, EFTYCHIOS and BARBIC, JERNEJ. "FEM simulation of 3D deformable solids: a practitioner's guide to theory, discretization and model reduction". *ACM SIGGRAPH 2012 Courses*. SIGGRAPH '12. Los Angeles, California: Association for Computing Machinery, 2012. DOI: 10.1145/2343483.2343501 6, 14.

[SHM23] SHAO, HAN, HUANG, LIBO, and MICHELS, DOMINIK L. "A Current Loop Model for the Fast Simulation of Ferrofluids". *IEEE Transactions on Visualization and Computer Graphics* 29.12 (2023), 5394–5405. DOI: 10.1109/TVCG.2022.3211414 2, 9, 10, 16, 17.

[SMB01] SERPICO, C., MAYERGOYZ, I. D., and BERTOTTI, G. "Numerical technique for integration of the Landau–Lifshitz equation". *Journal of Applied Physics* 89.11 (June 2001), 6991–6993. DOI: 10.1063/1.1358818 8.

[SNZ*21] SUN, YUCHEN, NI, XINGYU, ZHU, BO, et al. "A material point method for nonlinearly magnetized materials". *ACM Trans. Graph.* 40.6 (Dec. 2021). DOI: 10.1145/3478513.3480541 1, 2, 10, 11, 15, 18, 19.

[SS11] SAUTER, STEFAN A. and SCHWAB, CHRISTOPH. "Boundary Element Methods". *Boundary Element Methods*. Berlin, Heidelberg: Springer Berlin Heidelberg, 2011, 183–287. DOI: 10.1007/978-3-540-68093-2 11.

[SS86] SAAD, YOUCEF and SCHULTZ, MARTIN H. "GMRES: A Generalized Minimal Residual Algorithm for Solving Nonsymmetric Linear Systems". *SIAM Journal on Scientific and Statistical Computing* 7.3 (1986), 856–869. DOI: 10.1137/0907058 11.

[SSC*13] STOMAKHIN, ALEXEY, SCHROEDER, CRAIG, CHAI, LAWRENCE, et al. "A material point method for snow simulation". *ACM Trans. Graph.* 32.4 (July 2013). DOI: 10.1145/2461912.2461948 2.

[Sta99] STAM, JOS. "Stable fluids". *Proceedings of the 26th Annual Conference on Computer Graphics and Interactive Techniques*. SIGGRAPH '99. USA: ACM Press/Addison-Wesley Publishing Co., 1999, 121–128. DOI: 10.1145/311535.311548 1.

[TC20] TONG, MEI SONG and CHEW, WENG CHO. *The Nyström Method in Electromagnetics*. Singapore: John Wiley & Sons, 2020. DOI: 10.1002/9781119284857 11.

[TF88] TERZOPOULOS, DEMETRI and FLEISCHER, KURT. "Modeling inelastic deformation: viscolelasticity, plasticity, fracture". *Proceedings of the 15th Annual Conference on Computer Graphics and Interactive Techniques*. SIGGRAPH '88. New York, NY, USA: Association for Computing Machinery, 1988, 269–278. DOI: 10.1145/54852.378522 2.

[TGPS08] THOMASZEWSKI, BERNHARD, GUMANN, ANDREAS, PABST, SIMON, and STRASSER, WOLFGANG. "Magnets in motion". *ACM Trans. Graph.* 27.5 (Dec. 2008). DOI: 10.1145/1409060.1409115 1, 2, 7, 8, 12, 13.

[TPBF87] TERZOPOULOS, DEMETRI, PLATT, JOHN, BARR, ALAN, and FLEISCHER, KURT. "Elastically deformable models". *Proceedings of the 14th Annual Conference on Computer Graphics and Interactive Techniques*. SIGGRAPH '87. New York, NY, USA: Association for Computing Machinery, 1987, 205–214. DOI: 10.1145/37401.37427 1.

[Wei12] WEISCHEDEL, CLARISSE. "A discrete geometric view on shear-deformable shell models". PhD thesis. Göttingen, Niedersachsen, Germany: Georg-August-Universität Göttingen, 2012. DOI: 10.53846/goediss-2453 6.

[WFJB24] WESTHOFEN, LUKAS, FERNÁNDEZ-FERNÁNDEZ, JOSÉ A., JESKE, STEFAN R., and BENDER, JAN. "Strongly Coupled Simulation of Magnetic Rigid Bodies". *Computer Graphics Forum* 43.8 (2024), e15185. DOI: 10.1111/cgf.15185 1, 2, 7, 13, 18.

[WKGZ20] WANG, LIU, KIM, YOONHO, GUO, CHUAN FEI, and ZHAO, XUANHE. "Hard-magnetic elastica". *Journal of the Mechanics and Physics of Solids* 142 (2020), 104045. DOI: 10.1016/j.jmps.2020.104045 14.

[YCE*16] YETISEN, ALI K., COSKUN, AHMET F., ENGLAND, GRANT, et al. "Art on the Nanoscale and Beyond". *Advanced Materials* 28.9 (2016), 1724–1742. DOI: 10.1002/adma.201502382 16.

[YHY*21] YAN, YOUCAN, HU, ZHE, YANG, ZHENGBAO, et al. "Soft magnetic skin for super-resolution tactile sensing with force self-decoupling". *Science Robotics* 6.51 (2021), eabc8801. DOI: 10.1126/scirobotics.abc8801 19.

[YPC*21] YAN, DONG, PEZZULLA, MATTEO, CRUVEILLER, LILIAN, et al. "Magneto-active elastic shells with tunable buckling strength". *Nature communications* 12.1 (2021), 1–9. DOI: 10.1038/s41467-021-22776-y 14.

[YSS*24] YAN, YIMO, SONG, CHAO, SHEN, ZAIYI, et al. "Programming structural and magnetic anisotropy for tailored interaction and control of soft microrobots". *Communications Engineering* 3.7 (2024). DOI: 10.1038/s44172-023-00145-5 19.

[YSSP22] YAN, YOUCAN, SHEN, YAJING, SONG, CHAOYANG, and PAN, JIA. "Tactile Super-Resolution Model for Soft Magnetic Skin". *IEEE Robotics and Automation Letters* 7.2 (2022), 2589–2596. DOI: 10.1109/LRA.2022.3141449 19.

[ZB05] ZHU, YONGNING and BRIDSON, ROBERT. "Animating sand as a fluid". *ACM Trans. Graph.* 24.3 (July 2005), 965–972. DOI: 10.1145/1073204.1073298 2, 19.

[ZCJC24] ZHANG, JUNJIE, CHEN, GUANGYUAN, JIN, ZHENHU, and CHEN, JIAMIN. "A Review on Magnetic Smart Skin as Human–Machine Interfaces". *Advanced Electronic Materials* 10.5 (2024), 2300677. DOI: 10.1002/aelm.202300677 19.

[ZKC*19] ZHAO, RUIKE, KIM, YOONHO, CHESTER, SHAWN A., et al. "Mechanics of hard-magnetic soft materials". *Journal of the Mechanics and Physics of Solids* 124 (2019), 244–263. DOI: 10.1016/j.jmps.2018.10.008 14, 19.

[ZSYZ19] ZHANG, XIAOXUAN, SUN, LINGYU, YU, YUNRU, and ZHAO, YUANJIN. "Flexible Ferrofluids: Design and Applications". *Advanced Materials* 31.51 (2019), 1903497. DOI: 10.1002/adma.201903497 15.

[ZZX*24] ZHOU, YIHAO, ZHAO, XUN, XU, JING, et al. "A multimodal magnetoelastic artificial skin for underwater haptic sensing". *Science Advances* 10.1 (2024), eadj8567. DOI: 10.1126/sciadv.adj8567 19.

**Appendix A:** Sharp versus Smoothed Magnetic Interfaces

This section quantifies the modeling error incurred when a physically sharp jump in magnetic permeability is replaced by a diffuse transition layer of thickness $\varepsilon$ in numerical schemes (e.g., smoothed-Heaviside or diffuse-interface formulations). Using a minimal ferrohydrodynamic stability problem as a testbed, previously analyzed by Cowley and Rosensweig [CR67] and Abou et al. [ADW97], we (i) recover the sharp-interface dispersion relation from a standard Maxwell-stress calculation, and (ii) perform a matched expansion for a generic regularized profile $\mu_r(z)$ across the interface. The key result is that smoothing generically contaminates the normal magnetic pressure at $O(\varepsilon)$ (equivalently $O(k\varepsilon)$ in the dispersion relation), unless the regularization is centered so as to preserve the sharp-interface symmetry.

**Sharp interface.** We consider an incompressible magnetic liquid of infinite depth occupying $z < \zeta(x,t)$, with density $\rho$ and surface tension $\gamma$, under gravity $\boldsymbol{g}$ and a uniform imposed vertical field $\boldsymbol{H}_0 = H_0\hat{\boldsymbol{z}}$. Irrotational flow, $\boldsymbol{v} = \boldsymbol{\nabla}\Phi$, implies

$$\boldsymbol{\nabla}^2\Phi = 0, \tag{85}$$

with a decaying plane-wave ansatz

$$\Phi(x,z,t) = A\,\mathrm{e}^{kz}\mathrm{e}^{\mathrm{i}(kx-\omega t)}, \qquad z < \zeta, \tag{86}$$

and interface perturbation

$$\zeta(x,t) = s + \zeta_0\mathrm{e}^{\mathrm{i}(kx-\omega t)}, \qquad k\zeta_0 \ll 1. \tag{87}$$

The kinematic boundary condition at $z = 0$ gives

$$\frac{\partial\zeta}{\partial t} = \left.\frac{\partial\Phi}{\partial z}\right|_{z=0} \quad\Rightarrow\quad -\mathrm{i}\omega\zeta_0 = kA. \tag{88}$$

The linearized dynamic boundary condition reads

$$\rho\left.\frac{\partial\Phi}{\partial t}\right|_{z=0} = -\rho g\zeta + \gamma\boldsymbol{\nabla}^2\zeta + p_{\mathrm{m}}, \tag{89}$$

where $p_{\mathrm{m}}$ is the normal magnetic pressure jump.

In magnetostatics $\boldsymbol{H} = -\boldsymbol{\nabla}\phi_{\mathrm{tot}}$ and $\boldsymbol{\nabla}\cdot\boldsymbol{B} = 0$ imply

$$\boldsymbol{\nabla}\cdot(\mu\,\boldsymbol{\nabla}\phi_{\mathrm{tot}}) = 0, \tag{90}$$

with $\mu = \mu_0$ for $z > \zeta$ and $\mu = \mu_r\mu_0$ for $z < \zeta$. The unperturbed fields are uniform, with magnitudes $H_0$ above and $H_0/\mu_r$ below. The linear solutions are therefore

$$\phi_{\mathrm{tot}}(x,z,t) = \begin{cases} -H_0 z + a\mathrm{e}^{-kz}\mathrm{e}^{\mathrm{i}(kx-\omega t)}, & z > \zeta, \\ -\dfrac{H_0}{\mu_r}z + b\mathrm{e}^{kz}\mathrm{e}^{\mathrm{i}(kx-\omega t)}, & z < \zeta. \end{cases} \tag{91}$$

Imposing continuity of tangential $\boldsymbol{H}$ and normal $\boldsymbol{B}$ at $z = \zeta$ to $O(\zeta_0)$ yields

$$-H_0\zeta_0 + a = -\frac{H_0}{\mu_r}\zeta_0 + b, \qquad -H_0 - ka = -H_0 + \mu_r kb, \tag{92}$$

hence

$$a = -\mu_r b = \frac{\mu_r - 1}{\mu_r + 1}H_0\zeta_0. \tag{93}$$

Using Eq. (74), the magnetic pressure jump expanded to first order in $\zeta_0$ is

$$p_{\mathrm{m}} = \frac{\mu_r - 1}{2\mu_r}\mu_0 H_0^2 + \frac{(\mu_r - 1)^2}{\mu_r(\mu_r + 1)}\mu_0 k H_0^2\,\zeta_0, \tag{94}$$

where the constant term is balanced by the mean elevation $s$. Substitution into the dynamic condition gives the sharp-interface dispersion relation

$$\rho\omega^2 = \rho g k + \gamma k^3 - \frac{(\mu_r - 1)^2}{\mu_r(\mu_r + 1)}\mu_0 k^2 H_0^2. \tag{95}$$

At onset ($\omega = 0$) one obtains

$$\rho g + \gamma k^2 - \kappa\mu_0 k H_0^2 = 0, \qquad \kappa = \frac{(\mu_r - 1)^2}{\mu_r(\mu_r + 1)}, \tag{96}$$

and minimizing $H_0^2(k)$ yields the critical field

$$H_{\mathrm{c}}^2 = \frac{2\sqrt{\rho g\gamma}}{\kappa\mu_0}. \tag{97}$$

**Diffuse interface and leading error.** We now replace the jump in $\mu_r$ by a smooth profile $\mu_r(z)$ transitioning over a layer of thickness $\varepsilon \ll \zeta_0$ (cf. Eq. (59)). Within the layer, $\boldsymbol{\nabla}\cdot(\mu_r\boldsymbol{\nabla}\phi_{\mathrm{tot}}) = 0$ no longer reduces to a constant-coefficient equation. Writing

$$\phi_{\mathrm{tot}}(z) = \alpha + \beta(z)\mathrm{e}^{\mathrm{i}(kx-\omega t)} - \int_{\zeta}^{z}\frac{H_0}{\mu_r(z)}\,\mathrm{d}z, \tag{98}$$

the perturbation amplitude satisfies

$$\frac{\mathrm{d}}{\mathrm{d}z}(\mu_r(z)\beta'(z)) - \mu_r(z)k^2\beta(z) = 0. \tag{99}$$

Because $\beta = O(\zeta_0)$ varies across a thickness $\varepsilon$, one has $\beta' = O(\zeta_0/\varepsilon)$, so terms involving $\mu_r' = O(1/\varepsilon)$ enter at leading order. A consistent inner expansion is therefore

$$\mu_r(z)\beta'(z) = \frac{C_0}{\varepsilon} + kC_1 + C_2k^2(z - \zeta), \tag{100}$$

and hence

$$\begin{aligned}\beta(z) = \beta_0 &+ \int_{\zeta}^{z}\frac{C_0}{\varepsilon\,\mu_r(s)}\,\mathrm{d}s \\ &+ k\int_{\zeta}^{z}\frac{C_1}{\mu_r(s)}\,\mathrm{d}s + k^2\int_{\zeta}^{z}\frac{C_2(s-\zeta)}{\mu_r(s)}\,\mathrm{d}s.\end{aligned} \tag{101}$$

Matching to outer solutions of the form

$$\phi_{\mathrm{tot}}(x,z,t) = \begin{cases} -H_0 z + \left(a + k\varepsilon\,a^{(1)} + k^2\varepsilon^2 a^{(2)}\right)\mathrm{e}^{-kz}\mathrm{e}^{\mathrm{i}(kx-\omega t)}, \\ -\dfrac{H_0}{\mu_r}z + \left(b + k\varepsilon\,b^{(1)} + k^2\varepsilon^2 b^{(2)}\right)\mathrm{e}^{kz}\mathrm{e}^{\mathrm{i}(kx-\omega t)}, \end{cases} \tag{102}$$

gives, at leading order,

$$a + \mu_r b = 0, \tag{103}$$

as in the sharp problem, but the first correction involves permeability-weighted moments of the inner solution and is generically nonzero:

$$a^{(1)} + \mu_r b^{(1)} = -\frac{1}{\varepsilon}\int_{\zeta-\varepsilon}^{\zeta+\varepsilon}\mu_r(z)\left(\beta_0 + \int_{\zeta}^{z}\frac{C_0}{\mu_r(s)\varepsilon}\,\mathrm{d}s\right)\mathrm{d}z. \tag{104}$$

This term is precisely the mechanism by which smoothing introduces an $O(\varepsilon)$ shift in the matched amplitudes and, through

Eq. (74), an $O(\varepsilon)$ error in $p_{\mathrm{m}}$ (hence an $O(k\varepsilon)$ error in the dispersion relation and inferred threshold).

The $O(\varepsilon)$ contribution cancels only if the regularization preserves the sharp-interface symmetry, i.e., if the transition is centered so that $\mu_{\mathrm{r}}(z)$ is (up to constant prefactors on each side) an even function about $z = \zeta$. A generic smooth interpolation between $\mu_{\mathrm{r}} = 1$ and $\mu_{\mathrm{r}} = \text{const}$ need not satisfy this centering condition, making the cancellation nontrivial.

**Consistency check with sharp interface.** For the original discontinuous interface, one finds

$$\frac{1}{\varepsilon}\int_{\zeta-\varepsilon}^{\zeta+\varepsilon} \mu_{\mathrm{r}}^{-1}(z)\,\mathrm{d}z = 1 + \frac{1}{\mu_{\mathrm{r}}}, \tag{105}$$

so that

$$C_0 = \mu_{\mathrm{r}}\frac{a-b}{1+\mu_{\mathrm{r}}}, \qquad \beta_0 = \frac{a+\mu_{\mathrm{r}}b}{1+\mu_{\mathrm{r}}} = 0. \tag{106}$$

The permeability-weighted integral entering the matching condition then becomes

$$\begin{aligned} a^{(1)} + \mu_{\mathrm{r}} b^{(1)} = &-\frac{1}{\varepsilon}\int_{\zeta}^{\zeta+\varepsilon}\left(\beta_0 + C_0\frac{z-\zeta}{\varepsilon}\right)\mathrm{d}z \\ &-\frac{1}{\varepsilon}\int_{\zeta-\varepsilon}^{\zeta}\mu_{\mathrm{r}}\left(\beta_0 + \frac{C_0}{\mu_{\mathrm{r}}}\frac{z-\zeta}{\varepsilon}\right)\mathrm{d}z, \end{aligned} \tag{107}$$

which evaluates to

$$a^{(1)} + \mu_{\mathrm{r}} b^{(1)} = -(\mu_{\mathrm{r}}+1)\beta_0 = 0. \tag{108}$$

Thus, a hard interface produces no first-order correction.

**Implication for simulations.** In practice, diffuse-interface or smoothed-Heaviside regularizations of the magnetic permeability are often introduced for numerical robustness, in order to alleviate the stiffness associated with a discontinuous jump in material properties. The present analysis shows that such regularizations modify the interfacial Maxwell stress at $O(\varepsilon)$, with the correction controlled by the structure of the transition layer. The sharp-interface result is recovered in the limit $\varepsilon \to 0$, or when the regularization preserves the symmetry of the discontinuous problem.

## Appendix B: Error Induced by a Finite Neumann Boundary

In this section, we quantify the error incurred when the open magnetostatic boundary condition, defined by decay at infinity, is approximated by a homogeneous Neumann condition imposed at a finite radius. As an analytically tractable model, we consider a linearly magnetizable sphere placed in a uniform applied magnetic field. By comparing the induced response obtained from the exact infinite-domain solution with that resulting from a finite-radius Neumann truncation, we derive a closed-form expression for the relative error. In the asymptotic limit $R_2 \gg R_1$, the truncation error is shown to scale as $O((R_1/R_2)^3)$.

We consider a sphere of radius $R_1$, composed of a linear magnetic material with permeability $\mu_{\mathrm{r}}\mu_0$, placed in a uniform external magnetic field $\boldsymbol{H}_{\mathrm{ext}} = H_0\hat{\boldsymbol{z}}$. In the absence of free currents, the magnetic field can be expressed as $\boldsymbol{H}_{\mathrm{int}} = -\boldsymbol{\nabla}\phi$, where the scalar potential satisfies Laplace's equation,

$$\boldsymbol{\nabla}^2\phi = 0. \tag{109}$$

Owing to axial symmetry about the $z$ axis, the scalar potential admits the multipole expansion

$$\begin{cases} \phi_1 = \sum_{l=0}^{\infty}\left(A_l r^l + B_l r^{-(l+1)}\right)P_l(\cos\theta), & r \le R_1, \\ \phi_2 = \sum_{l=0}^{\infty}\left(C_l r^l + D_l r^{-(l+1)}\right)P_l(\cos\theta), & r > R_1, \end{cases} \tag{110}$$

where $P_l$ denotes the Legendre polynomial of degree $l$. Regularity at the origin requires $B_l = 0$, and the gauge freedom of $\phi$ is fixed by setting $A_0 = C_0 = 0$. The applied field corresponds to the scalar potential $\phi_0 = -H_0 r P_1(\cos\theta)$.

At the material interface $r = R_1$, continuity of the tangential component of $\boldsymbol{H}$ and the normal component of $\boldsymbol{B}$ yields

$$\begin{aligned} \mu_0\left.\frac{\partial(\phi_1+\phi_0)}{\partial r}\right|_{r=R_1} &= \mu_{\mathrm{r}}\mu_0\left.\frac{\partial(\phi_2+\phi_0)}{\partial r}\right|_{r=R_1}, \\ \left.\frac{\partial\phi_1}{\partial\theta}\right|_{r=R_1} &= \left.\frac{\partial\phi_2}{\partial\theta}\right|_{r=R_1}. \end{aligned} \tag{111}$$

**Open boundary at infinity.** Imposing decay of the magnetic field at infinity requires $C_l = 0$ for all $l$. Substitution into Eq. (111) and projection onto individual Legendre modes yields $D_0 = 0$ and, after straightforward algebra,

$$\begin{cases} A_1 - H_0 = \mu_{\mathrm{r}}(-2D_1R_1^{-3} - H_0), \\ A_1R_1 = D_1R_1^{-2}, \end{cases} \tag{112}$$

together with, for all $l \ge 2$,

$$\begin{cases} lA_lR_1^{l-1} = -\mu_{\mathrm{r}}(l+1)D_lR_1^{-(l+2)}, \\ A_lR_1^{l} = D_lR_1^{-(l+1)}. \end{cases} \tag{113}$$

The solution is

$$A_1 = -\frac{\mu_{\mathrm{r}}-1}{2\mu_{\mathrm{r}}+1}H_0, \qquad D_1 = -\frac{\mu_{\mathrm{r}}-1}{2\mu_{\mathrm{r}}+1}H_0R_1^3, \tag{114}$$

with all higher-order multipoles vanishing identically,

$$A_l = 0, \qquad D_l = 0, \qquad \forall\, l \ge 2. \tag{115}$$

**Homogeneous Neumann boundary at $r = R_2$.** We now replace the open boundary by a homogeneous Neumann condition,

$$\left.\frac{\partial\phi_2}{\partial r}\right|_{r=R_2} = 0, \tag{116}$$

which enforces

$$D_0 = 0, \qquad lC_lR_2^{l-1} - (l+1)D_lR_2^{-(l+2)} = 0, \quad l \ge 1. \tag{117}$$

Together with the interface conditions at $r = R_1$, the resulting linear system for the dipolar mode yields

$$A_1 = \left(\frac{1}{R_1^3} + \frac{2}{R_2^3}\right)D_1, \qquad D_1 = -\frac{\mu_{\mathrm{r}}-1}{\frac{2\mu_{\mathrm{r}}+1}{R_1^3} - 2\frac{\mu_{\mathrm{r}}-1}{R_2^3}}H_0, \tag{118}$$

while all higher-order coefficients again vanish identically.

**Relative error.** Comparing the dipolar coefficients obtained from the two outer-boundary conditions, the relative error introduced by the finite-radius Neumann boundary is

$$\frac{D_{1,\mathrm{Neu}} - D_{1,\infty}}{D_{1,\infty}} = \frac{2\frac{\mu_r - 1}{R_2^3}}{\frac{2\mu_r + 1}{R_1^3} - 2\frac{\mu_r - 1}{R_2^3}} \sim O\left(\frac{R_1^3}{R_2^3}\right), \tag{119}$$

demonstrating that the truncation error induced by a homogeneous Neumann boundary decays cubically with the ratio $R_1/R_2$ in the limit $R_2 \gg R_1$.

This result provides a quantitative *a priori* estimate for the finite-domain error introduced by magnetic shielding boundary conditions in numerical simulations. In particular, achieving a prescribed relative accuracy $\varepsilon$ in the induced dipolar response requires $R_2/R_1 \gtrsim \varepsilon^{-1/3}$.